



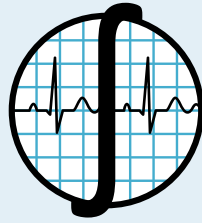
Una publicación de:  
**SOMIB**  
Sociedad Mexicana  
de Ingeniería Biomédica

# ib

## Revista Mexicana de Ingeniería Biomédica

### **New publishing model**

*Continuous publication:*  
**once a manuscript is accepted and  
prepared, it will be released online**



**SOMIB**  
Sociedad Mexicana  
de Ingeniería Biomédica

# Sociedad Mexicana de Ingeniería Biomédica



Si aún no formas parte de la SOMIB, inscríbete ya. Tendrás muchísimas experiencias y aplicaciones útiles en tu vida profesional: cada año, participamos en varios eventos relacionados con la Ingeniería Biomédica; te ofrecemos descuentos de hasta 50% en cursos, congresos y eventos organizados por la SOMIB; una vez inscrito, puedes contar con una credencial de la Sociedad; y, además, si deseas incluir un anuncio para la bolsa de trabajo en el sitio Web de SOMIB, te ofrecemos un 50% de descuento si eres socio con membresía empresarial. Cada inscripción anual incluye los tres números de la Revista Mexicana de Ingeniería Biomédica que edita la SOMIB.

## INSCRIPCIONES 2017

### Personal

PROFESIONISTA:

**\$1,160.00**

ESTUDIANTE:

**\$683.00**

### Grupal

6 A 10 PERSONAS:

**10% de descuento**

11 O MÁS PERSONAS:

**15% de descuento**

### Institucional:

**\$9,860.00**

## PUBLICIDAD

Contiene el logotipo de la empresa, un link a su página Web y cuatro membresías.

MEDIA PLANA:

**\$4,964.70**

UNA PLANA:

**\$6,388.80**

CONTRAPORTADA:

**\$7,719.80**

FORROS INTERIORES:

**\$7,719.80**

LOS COSTOS NO INCLUYEN I.V.A.

## Publicación en SOMIB Web

[www.somib.org.mx](http://www.somib.org.mx)

## Proveedores

Contiene logotipo de la empresa y link a su página principal.

## Bolsa de trabajo

Ofertas exclusivas para Ingenieros Biomédicos.

## Publicación en RMIB Digital

[rmib.com.mx](http://rmib.com.mx)

## Artículos

Publicación de artículos originales de investigación y de divulgación.

## Anuncios Comerciales

Publicación de logotipo, servicios y productos que ofrece la empresa.

## INFORMES

Plaza Buenavista #2,  
Col. Buenavista  
Del. Cuauhtémoc, C.P. 06350  
Ciudad de México, México  
(555) 574-4505  
[rmib.somib@gmail.com](mailto:rmib.somib@gmail.com)  
[www.somib.org.mx](http://www.somib.org.mx)

**Fundador**  
Dr. Carlos García Moreira

**COMITÉ EDITORIAL**

**Editora en Jefe**  
Dra. Dora-Luz Flores  
UNIVERSIDAD AUTÓNOMA DE BAJA CALIFORNIA

**Editores Asociados Nacionales**

**Dr. Christian Chapa González**  
UNIVERSIDAD AUTÓNOMA DE CIUDAD JUÁREZ

**Dra. en C. Citlalli Jessica Trujillo Romero**  
DIVISIÓN DE INVESTIGACIÓN EN INGENIERÍA MÉDICA  
INSTITUTO NACIONAL DE REHABILITACIÓN "LUIS GUILLERMO IBARRA IBARRA"

**Dr. Rafael Eliecer González Landaeta**  
UNIVERSIDAD AUTÓNOMA DE CIUDAD JUÁREZ

**Dra. Rebeca Romo Vázquez**  
UNIVERSIDAD DE GUADALAJARA

**Dra. Isela Bonilla Gutiérrez**  
UNIVERSIDAD AUTÓNOMA DE SAN LUIS POTOSÍ

**Comité Editorial Internacional**

**Dr. Leonel Sebastián Malacrida Rodríguez**  
UNIVERSIDAD DE LA REPÚBLICA, URUGUAY

**Dra. Elisa Scalco**  
INSTITUTE OF BIOMEDICAL TECHNOLOGY  
ITALIAN NATIONAL RESEARCH COUNCIL, MILAN, ITALY

**Dra. Natali Olaya Mira**  
INSTITUTO TECNOLÓGICO METROPOLITANO  
ITM, MEDELLÍN, COLOMBIA

**Índices**

La Revista Mexicana de Ingeniería Biomédica aparece en los siguientes índices científicos:  
**Sistema de Clasificación de Revistas Científicas y Tecnologías del CONACYT - Q4, SCOPUS, SciELO, EBSCO, LATINDEX, Medigraphic Literatura Biomédica, Sociedad Iberoamericana de Información Científica - SIIC.**

[www.rmib.mx](http://www.rmib.mx)  
ISSN 2395-9126

**Asistente Editorial**  
Carla Ivonne Guerrero Robles

**Editor Técnico y en Internet**  
Sandra Sánchez Jáuregui

Se autoriza la reproducción parcial o total de cualquier artículo a condición de hacer referencia bibliográfica a la Revista Mexicana de Ingeniería Biomédica y enviar una copia a la redacción de la misma.



**Sociedad Mexicana de Ingeniería Biomédica**

Juan Vázquez de Mella #481, Polanco I Sección, Alc. Miguel Hidalgo, C. P. 11510, Ciudad de México, México, (555) 574-4505



**SOMIB**  
Sociedad Mexicana  
de Ingeniería Biomédica

### **MESA DIRECTIVA**

**Ing. Francisco Javier Aceves Aldrete**

PRESIDENTE

**Mtra. Natalia Gabriela Sámano Lira**

VICEPRESIDENTA

**Mtra. Verónica Guadalupe Castillo Sánchez**

TESORERA

**Ing. Janette Mariana Tarín León**

SECRETARÍA GENERAL

**Dra. Dora-Luz Flores**

EDITORA EN JEFE DE RMIB

### **Afiliada a:**

International Federation of Medical and Biological Engineering (IFMB-IUPSM-ICSU)  
Federación de Sociedades Científicas de México, A.C. (FESOCIME)  
Consejo Regional de Ingeniería Biomédica para América Latina (CORAL)

### **SOMIB**

Juan Vázquez de Mella #481, Polanco I Sección, Alc. Miguel Hidalgo, C. P. 11510, Ciudad de México, México (555) 574-4505

[www.somib.org.mx](http://www.somib.org.mx)

**REVISTA MEXICANA DE INGENIERÍA BIOMÉDICA**, Vol. 43, No. 2, Mayo-Agosto 2022, es una publicación cuatrimestral editada por la Sociedad Mexicana de Ingeniería Biomédica A.C., Juan Vázquez de Mella #481, Polanco I Sección, Alc. Miguel Hidalgo, C. P. 11510, Ciudad de México, México, (555) 574-4505, [www.somib.org.mx](http://www.somib.org.mx), [rmib.somib@gmail.com](mailto:rmib.somib@gmail.com). Editora responsable: Dra. Dora-Luz Flores. Reserva de Derechos al Uso Exclusivo No. 04-2015-041310063800-203, ISSN (impreso) 0188-9532; ISSN (electrónico) 2395-9126, ambos otorgados por el Instituto Nacional del Derecho de Autor. Responsable de la última actualización de este número: Lic. Enrique Federico Ban Sánchez, Juan Vázquez de Mella #481, Polanco I Sección, Alc. Miguel Hidalgo, C. P. 11510, Ciudad de México, México, (555) 574-4505, fecha de última modificación, 20 de abril de 2022.

El contenido de los artículos, así como las fotografías son responsabilidad exclusiva de los autores. Las opiniones expresadas por los autores no necesariamente reflejan la postura del editor de la publicación.

Queda estrictamente prohibida la reproducción total o parcial de los contenidos e imágenes de la publicación sin previa autorización de la Sociedad Mexicana de Ingeniería Biomédica.

**Disponible en línea:**

[www.rmib.mx](http://www.rmib.mx)

**CONTENTS****CONTENIDO****Contents**

p 5

**Research Article**

p 44

**Research Article**

p 6

**Vaginal Electrical Impedance Detects the Fertile Window in Healthy Women: a Pilot Study***La Impedancia Eléctrica Vaginal Detecta la Ventana Fértil en Mujeres Sanas: un Estudio Piloto***Detection of People Positive to COVID-19 through ATR-FTIR Spectra Analysis of Saliva using Machine Learning***Detección de Personas Positivas a COVID-19 mediante el Análisis de Espectros ATR-FTIR de Muestras de Saliva empleando Machine Learning***Research Article**

p 15

**Segmentation of OCT and OCT-A Images using Convolutional Neural Networks***Segmentación de imágenes de OCT y OCT-A por medio de Redes Neuronales Convolucionales***Research Article**

p 25

**Electrical Impedance Tomography to Measure Spirometry Parameters in Chronic Obstructive Pulmonary Disease Patients***Tomografía por Impedancia Eléctrica para Medir Parámetros de Espirometría en Pacientes con Enfermedad Pulmonar Obstructiva Crónica***Book Review** p 36**Reseña del Libro: “Medicine-Based Informatics and Engineering” Lecture Notes in Bioengineering, Springer, 2022***Book Review: “Medicine-Based Informatics and Engineering” Lecture Notes in Bioengineering, Springer, 2022*

[dx.doi.org/10.17488/RMIB.43.3.1](https://doi.org/10.17488/RMIB.43.3.1)

E-LOCATION ID: 1290

## Vaginal Electrical Impedance Detects the Fertile Window in Healthy Women: a Pilot Study

### La Impedancia Eléctrica Vaginal Detecta la Ventana Fértil en Mujeres Sanas: un Estudio Piloto

José Alfonso Cruz-Ramos<sup>1</sup> , Joe Klepich<sup>2</sup> , Martha Eloisa Ramos-Márquez<sup>1</sup> , Gerardo García-Gil<sup>3</sup> ,  
Luis Ilich Vladimir Guerrero-Linares<sup>3</sup> , Gabriela del Carmen López-Armas<sup>3</sup>  

<sup>1</sup>Universidad de Guadalajara, Centro Universitario de Ciencias de la Salud - México

<sup>2</sup>School of Informatics, master's in Information and Data Science, University of California, Berkeley - United States

<sup>3</sup>Centro de Enseñanza Técnica Industrial, Guadalajara, Jalisco - México

#### ABSTRACT

This work analyzes the electrical impedance (EI) measurement of cervical mucus (CM) using a device to determine the fertile window. In this prospective and longitudinal study, fourteen healthy women aged 18 to 44 were enrolled to evaluate three menstrual cycles. EI was measured through a medical device inserted into the vagina for two minutes daily. Patients were monitored by urine luteinizing hormone (LH) strip, blood collection, and vaginal ultrasound to visualize the dominant follicle. Finally, the predictive EI capacity was validated by the receiver operating characteristic (ROC) of anovulatory vs. ovulatory impedances. The peak of LH was 35.7 ( $\pm 4.5$ ) mUI/ml and the dominant follicle size was 15.45 mm ( $\pm 0.559$ ). There were statistical differences in EI measurements between the follicular and luteal phases vs. the ovulation phase ( $p < 0.0361$  and  $p < 0.0160$ ). After data normalization, an area under the ROC curve (AUC) of 0.713 (P value= 0.0253), a Youden J index of 0.4545 $\Omega$ , a sensitivity of 63.6%, and a specificity of 81.8% were found. Low EI in the ovulatory period belongs to the LH ovulatory peak and follicular release. EI can be used for ovulation monitoring, birth control, or promoting pregnancy as a safe and innocuous method.

**KEYWORDS:** Electrical impedance, cervical mucus, ovulation, luteinizing hormone

## RESUMEN

Este trabajo analiza la medición de la impedancia eléctrica (IE) del moco cervical (MC) mediante un dispositivo para determinar la ventana fértil. En este estudio prospectivo y longitudinal, se incluyeron 14 mujeres sanas de 18 a 44 años para evaluar tres ciclos menstruales. La IE se midió a través de un dispositivo médico colocado en la vagina durante dos minutos diarios. Las pacientes fueron monitoreadas con una tira de hormona luteinizante (LH) en orina, recolección de sangre y ultrasonido vaginal para visualizar el folículo dominante. Finalmente, la capacidad predictiva de IE fue validada por la curva ROC (*receiver operating characteristic*) de impedancias anovulatorias vs. ovulatorias. El pico de LH fue de 35.7(±4.5) mUI/ml; el folículo de tamaño dominante fue de 15.45 mm (±0.559). Se encontraron diferencias estadísticas para la medición de la IE de las fases folicular y lútea versus la fase de ovulación ( $p < 0.0361$  y  $p < 0.0160$ ). Después de la normalización de los datos, se encontró un área bajo la curva ROC (AUC) de 0.713 (valor de  $P = 0.0253$ ), un índice de Youden  $J$  de 0.4545  $\Omega$ , sensibilidad del 63.6 % y especificidad del 81.8 %. La IE baja en el período ovulatorio que pertenece al pico ovulatorio de LH y liberación folicular. La IE se puede utilizar para el control de la ovulación, el control de la natalidad o la promoción del embarazo como método seguro e inocuo.

**PALABRAS CLAVE:** Impedancia eléctrica, moco cervical, ovulación, hormona luteinizante

### Corresponding author

TO: Gabriela del Carmen López-Armas

INSTITUTION: Centro de Enseñanza Técnica Industrial

ADDRESS: Calle Nueva Escocia #1885, Col. Providencia

5ta. Sección, C. P. 44638, Guadalajara, Jalisco, México

CORREO ELECTRÓNICO: [glopez@ceti.mx](mailto:glopez@ceti.mx)

### Received:

20 June 2022

### Accepted:

18 August 2022

## INTRODUCTION

Cervical mucus (CM) is produced by secretory cells in endocervical glands and discharged into the endocervical conduct. CM is composed mostly of water (up to 90%); the rest consists of mucins that confer viscoelastic gel properties, amino acids, ions, cholesterol, lipids, glucose, polysaccharides, soluble proteins, and enzymes [1] [2] [3]. In normal conditions, the secretion of CM changes quantitatively and qualitatively through the hormonal cycle stage.

The secretion of CM depends on the hormonal cycle: women produce 20-60 mg of CM per day until they reach approximately 600 mg in the ovulation period, a crucial change for the transport of spermatozoa to the mature follicle [4]. This pattern occurs in fertile women, but in infertile females, the panorama is quite different [5]. Several hormones participate in ovulation: gonadotropin-releasing hormone (GnRH) acting from the hypothalamus; follicle-stimulating hormone (FSH) and luteinizing hormone (LH) secreted by the anterior pituitary gland, and estradiol and progesterone produced in the ovary. In the initial phase of the menstrual cycle, the estrogens stimulate FSH production and release; by positive feedback, FSH increases during the first half of the cycle. In the middle of the cycle, the rise in FSH and LH triggers ovulation [6]. Later, the surge in FSH and LH generates negative feedback in gonadotropin secretion, and the hormone levels fall during the second half of the cycle. If pregnancy is absent, the secretion of estrogens and progesterone starts to diminish after ovulation, and menstrual bleeding occurs. Hormonal fluctuations throughout the menstrual cycle are the main factor influencing ovulation [7].

Ovulation is currently detected through blood tests and intravaginal ultrasound to identify the dominant ovarian follicle [8]. EI has been widely used in biological applications since 1925, with significant advances during the past one hundred years [9] [10] [11]; actually, it may be a more reliable and convenient detection tool. Although EI has been used to assess cervical neoplasia or cervical

ripening in pregnant and non-pregnant women [12] [13] [14], it has barely been applied to detect ovulation [15] [16] [17] [18] [19] [20]. Hence, this work aims to determine the ovulation window via measuring the impedance of CM by a minimum invasive EI device. Our principal objective was to assess the feasibility of correlating impedance values with serum concentrations of estradiol, FSH, LH, progesterone, prolactin, and total testosterone, as well as intravaginal ultrasound, to observe and measure ovarian follicle release. All laboratory tests were performed according to each patient menstrual cycle to precisely detect the ovulation period or fertile window.

## MATERIALS AND METHODS

This pilot, prospective, longitudinal protocol aimed to identify variations of EI in cervical mucus at different phases of the reproductive cycle. Fourteen healthy women aged from 18 to 44 years and with a complete gynecological-obstetric history were included. Each participant provided written consent for blood procedure, intravaginal ultrasound, and device use. Internal Committee for Research and Follow-up of Research Projects (CIESPI) of the Technical Industrial Teaching Center approved the study with the number PI-07-18-20. All selected participants had a normal hormonal profile, did not use hormonal contraceptives, DIU dispositive, or any vaginal treatment such as lubricants, creams, or ointments for at least two months, and were willing to take protective measures during sexual intercourse. All women had regular pap smear reports. During the study, two participants were excluded by a hormonal disturbance in the second cycle and another one for pregnancy, staying only eleven. With prior training for device and mobile app use, all women auto-measured impedance with the Kegg device for two minutes daily in the morning. Measurements were made for three consecutive menstrual cycles starting the first day after bleeding in each cycle. The hormonal activity was monitored in urine, blood samples, and ovulation via vaginal ultrasound (Figure 1- c). For the correct use of the device, the dorsal position was obligatory.



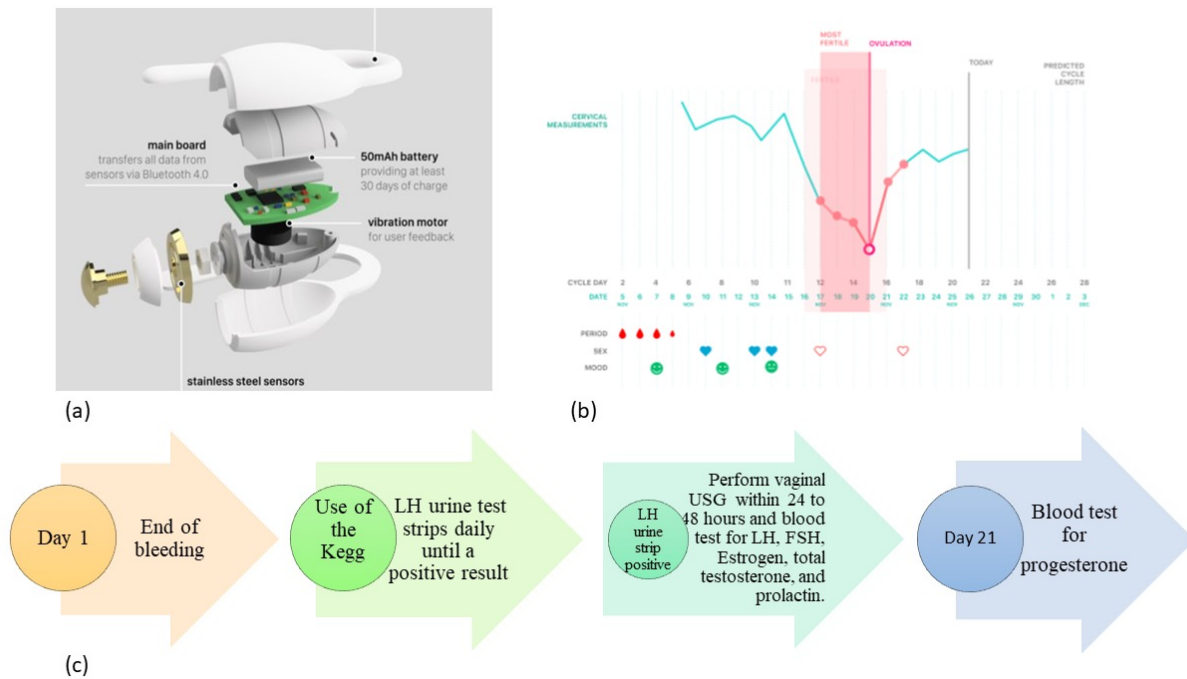


**FIGURE 1. (a) Keggt™ device for EI measurement of CM. (b) The mobile application data register. (c) Timeline. Arrow 1. All subjects must finish vaginal bleeding to start measuring impedance. Arrow 2. All participants began to use the LH strip until getting a positive result and continued using the device. Arrow 3. Serum quantification of hormones in the blood once positive urine strip: LH, FSH, Estrogen, total testosterone, and prolactin. Vaginal ultrasound performed within 24 to 48 hours after LH peak. Arrow 4. Serum quantification of progesterone. This scheme was repeated for three menstrual cycles.**

### Electric impedance measurement

We used kegg device, model K-1 (Lady Technologies, Inc., San Francisco, CA), powered by a 50mAh battery that includes an electronic impedance circuit made with gold-plated stainless-steel electrodes, a main-board to transfer all information via Bluetooth to mobile application (Android and IOS) and a vibration motor for patient feedback. The device is covered with medical-grade silicone for safety and comfortability and has been thoroughly tested according to IEC/ISO standards (Figure 1 a-b). For proper usage, the device is inserted into the vagina to reach the cervical fluid pool.

### Urine and blood sample hormonal measurements

On the same day the patients started using the EI device, they tested their LH concentration with the Clearblue® strip (S.P.D., Swiss Precision Diagnostics

GmbH, Geneve, Switzerland) on the first-morning urine daily. Once the strip test was positive, blood was collected by a venous puncture for hormonal determination of LH, FSH, estradiol, prolactin, and total testosterone employing immunoquimioluminiscence (Ortho, Vitros 5600, Inc. California, USA). Progesterone was determined in another blood sample by the same methodology on day 21 of each cycle.

### Vaginal ultrasound

The following day after the positive LH strip, the woman underwent a vaginal ultrasound (SonoAceR3, Samsung Health Care. Seoul, South Korea) to verify the amount and size of follicles in both ovaries.

### Characteristic of EI device

The impedance measurement of the kegg device is based on a balanced bridge whose voltage is read by the microprocessor ADC. The processor generates a 1

kHz signal at a known voltage which is used to excite one electrode (called the tip), the voltage is then read on the other electrode (called the ring) through an op-amp. This procedure is then reversed, whereby the second electrode is excited and read by the first. The processor performs a calculation based on the known values of the other legs of the bridge, and a reference value (excitation voltage) is then established to determine the resistance. The measurement is made multiple times to create a sample of set of 50 readings which is then averaged for a final impedance value.

The communication process is activated when the device receives a command from the mobile app via Bluetooth; fifty readings are required during a single measurement session. These readings are transferred to an Android mobile app via Bluetooth Low Energy; then, the data are saved on the cloud and processed to determine which readings fall within the fiftieth percentile and calculate a median value labeled as the final impedance value. These values are entered into the database for each user's session. The Bluetooth is turned off during the actual measurement process.

### Statistical Analysis

Data analysis was carried out using GraphPad Prism LLC version 8.01 software (San Diego, CA) and Medcalc software Ltd (Ostend, Belgium). Results are presented as means or medians. The raw impedance values of each phase were compared between them and to those of the other phases in the same woman and other subjects' values via the Mann-Whitney U test with Holm-Sidak correction and an alpha error of 0.05. The level of significance was set at  $P < 0.05$ . Data were normalized as follows:

The means of the impedance values of the follicular Equation 1 (FOL) and luteal Equation 2 (LUT) phases of each cycle were obtained with the following formula:

$$\underline{x_{FOL}} = \frac{x_1 + x_2 + x_n \dots}{n} \quad (1)$$

$$\underline{x_{LUT}} = \frac{x_1 + x_2 + x_n \dots}{n} \quad (2)$$

This means the impedance value of the day of ovulation (Impov) (LH peak) of the corresponding cycle was subtracted from Equations 3 and 4. The ovulation impedance values of 3 cycles were added, and the mean was obtained, which was subtracted from each individual ovulatory impedance measurement. Equation 5.

$$\underline{x_{FOL}} - Impov = \Delta_{FOL} \quad (3)$$

$$\underline{x_{LUT}} - Impov = \Delta_{LUT} \quad (4)$$

$$\Delta_{Impov} = x_{1Impov} - \underline{x_{Impov}} \quad (5)$$

With these values, multiple comparisons were made using the Friedman test and the ROC curve to compare the ovulatory phase against non-ovulatory phases (luteal and follicular).

## RESULTS AND DISCUSSION

No participants reported any injury or collateral effect using the device to measure impedance in cervical discharge or discomfort by venipuncture for blood tests.

### Subjects' metrics

Table 1 describes the mean age and standard deviation (SD) of the eleven participants at the beginning of the study, as well as blood values of LH, FSH, estradiol, prolactin, and total testosterone taken on ovulation day; only progesterone content was measured on day 21st of each menstrual cycle. Finally, to verify the ovulation, we also perform ultrasonography 24 to 48 hours after LH serum peak to visualize follicle size and number (Figure 2).

### CM raw impedance values

In total, there were 676 impedance measurements from cervical discharge from eleven participants. In Figure 3, we divided the menstrual cycle into three

phases: follicular, ovulatory (LH peak), and luteal. Our results show that the difference between follicular and ovulatory phases were statistically significant in impedance measurements (median 349.1Ω, and median 311.8Ω, P value= <0.0361) concerning the luteal phase vs. ovulatory phase (median 350.3Ω, and median 311.8Ω, P value= <0.016). Finally, we performed Holm-

**TABLE 1. Characteristics of the study subjects.**

Parameters	Values
Total participants (n)	11
Age (years)	30.6(±8.2)
LH (mUI/ml)	35.7 (±4.5)
Estradiol (pg/ml)	179.3 (±14.2)
Prolactin (ng/ml)	22.60 (±1.93)
Total Testosterone (ng/ml)	0.4109 (±0.025)

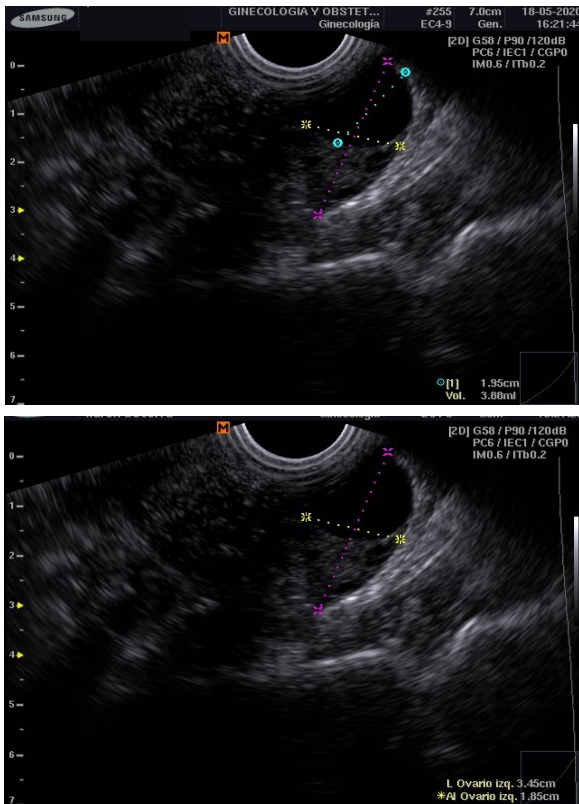


**FIGURE 2. Vaginal ultrasound of one patient.** Blue marks signal the dominant follicle of 1.95 cm. The yellow and purple marks represent the ovarian width and length in centimeters.

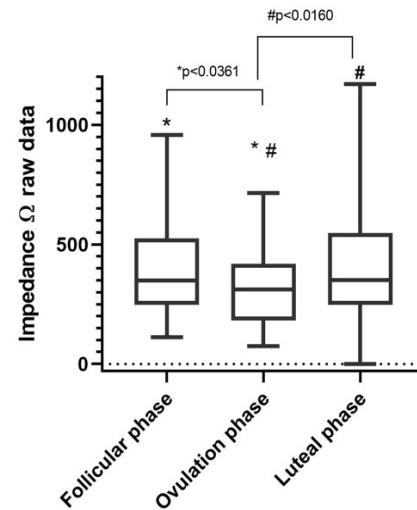


**FIGURE 3. Box and whisker plot. Impedance raw measure of follicular, ovulation, and luteal phases. (\*) Statistical differences were found in the impedance measurement of the follicular phase. U de Mann test.**

Sidak correction with an alpha of 0.05 for follicular and luteal phase comparisons against the ovulation phase (adjusted P value= <0.03 and adjusted P value= <0.02).

**CM normalized impedance values**

After data normalization, the Friedman test yielded a value of P = <0.0435 (Figure 4).

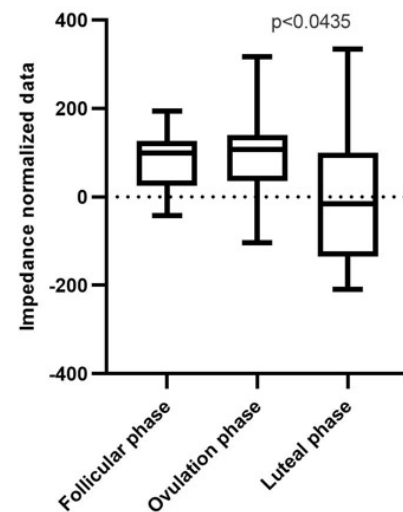


**FIGURE 4. Box and whisker plot. Impedance normalized data of follicular, ovulation, and luteal phases. (\*) Statistical differences were found for the impedance measurement between all phases (P < 0.0435)—Friedman test.**

To evaluate the device as a valuable method to distinguish the ovulation phase from follicular and luteal phases of the menstrual cycle, we obtained a receiver operating characteristic (ROC) curve under bootstrap confidence interval (1000 iterations; random number seed: 978), an area under the ROC curve (AUC) of 0.713 (value of  $p = <0.0253$ ), and a Youden index  $J$  of 0.4545 with a sensitivity of 63.64% and specificity of 81.82% (Figure 5). With these impedance measurements, we can discriminate between no ovulation period (follicular and luteal phases) and ovulation period (LH peak day).

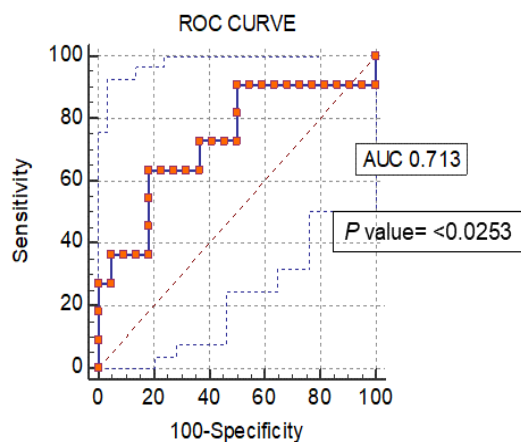


**FIGURE 5. ROC curves from normalized data of impedance measurements of the non-ovulation and ovulation (LH peak day) periods ( $p$  value=  $<0.0253$ ).**

This study describes the application of electrical impedance measurement to investigate conductivity changes in CM during the menstrual cycle in healthy women of reproductive age. Our results revealed a lower impedance during the ovulatory phase compared with the follicular and luteal phases. It is well known that pH changes in CM play a pivotal role in sperm survival since during the ovulation period, the mucus becomes less acidic with a nearly neutral pH, and sperm is thus protected, leading to changes in electrical impedance [21].

In this sense, some research has monitored the day-to-day changes in CM by EI devices. Previous reports measured salivary or vaginal electrical resistance (SER

or VER) with a CUE Fertility Monitor. In general, results show that the peak in LH occurred 4 to 5 days after the peak measurement in SER, and this had a strong positive correlation ( $r = 0.94$ ) with the urinary LH surge. As for VER values, these diminished along with the pre-ovulatory phase from day -3 until day 0. In this report, the VER mean at day 0 correlated with the LH surge; consequently, the nadir was the lowest value on the CUE Fertility Monitor. Moreno, *et al.* [13], concluded that CUE Fertility Monitor has potential for use in natural family planning (NFP). In contrast, a prospective study on the reliability of the CUE Fertility Monitor [22] that analyzed sixteen cycles with signals (i.e., SER and VER) for the beginning and the end of the fertile period, could not find signals in two cycles; therefore, the researchers did not recommend the CUE Fertility Monitor utilizing the current algorithm for NFP.

In this work, the EI device was used only once a day to measure CM. The main objective was to simplify the daily CM evaluation making it practical and comfortable for women. The results of this study indicate a low impedance value coincident with the LH peak and the appearance of the dominant follicle, as seen by ultrasonography. However, several factors mentioned below in order of importance can affect the impedances recorded by the device and should be considered by the end-user. First, end-users must follow the manufacturer's instructions for the Kegg device for two complete ovulatory cycles.

The methodology carried out in this study provides enough data to the APP for analysis. Second, it is necessary to constantly monitor the LH in urine or serum to determine a correlation between the impedance values obtained in the first three months when the LH test is positive. The observation of the LH peak and the impedance value is fundamental because each woman has her own hormonal rhythms that influence the composition of the mucus in the different phases, there are ultrastructural changes such as the increase

in pore size of the network of fibers that make up the mucus during the ovulatory phase that allows a greater flow of substances producing variations in resistivity and conductance [23]. Another factor is the water content of the mucus, which reaches up to 99% during ovulation, which has an impact on the decrease in impedance in this phase, as opposed to the follicular and luteal phases where the water content is 90 to 95%. Finally, mucus content and density may also have an influence, as there are noticeable changes in the follicular phase, with cervical mucus being more abundant and dense in the luteal phase compared to the ovulatory phase [24]. This last property depends on hydration, electrolyte content, exercise routine, nutritional habits, age, some vaginal infections, stressful conditions, etc. So, each woman needs to learn to know her hormonal levels and observe in time how they can affect CM production [25]. Third, in this study, users were asked to use protection in all sexual encounters to avoid direct contact of the device with the semen, as this could modify the impedance value. Once the proper cervical mucus values are gained, the recommendation is to allow 10-12 hours between the sexual encounter and the impedance measurement.

### CONCLUSIONS

This study shows that the kegg device, model K-1, helps to identify the LH ovulatory peak. Indeed, serum and urinary increases of LH, together with the ultrasonographic documentation of a dominant follicle, detect a woman's fertile window with a sensitivity of 63.6% and specificity of 81.8%. Measurement of CM electric impedance with the Kegg device is more reliable than daily monitoring of urinary LH test alone, making this method cost-effective along with the ease-of-use benefits. Further studies exploring different disorders (polycystic ovary syndrome, endometriosis, hyperprolactinemia, premature ovarian failure, or imbalance in thyroid hormone) that can affect the sensitivity and specificity of EI ovulation values are required.

### ETHICAL STATEMENT

This study followed the ethical principles regarding human experimentation proposed by the Helsinki declaration; all women were informed about the procedures, risks, and benefits to obtain the written consent of voluntary participation. The protocol was approved by the Internal Committee for Research and Follow-up of Research Projects (CIESPI) of the Technical Industrial Teaching Center with the number PI-07-18-20.

### CONFLICT OF INTEREST

Lady Technologies, Inc supported this project.

### ACKNOWLEDGMENT

Despite the health contingency, we are deeply grateful to each of the women who participated in this study and the health personnel of the different institutions. Also, we want to thank MD. Ma. de la Paz Jacinto-Orozco our OB/GYN of the protocol, Engr. Mario Antonio Mercado-Cisneros for all protocols communication between KEGG device and APP and Dr. Horacio Rivera-Ramírez for his review of the manuscript.

### AUTHOR CONTRIBUTIONS

J.A.C.R. performed formal analysis, carried out mathematical and statistical methods for the analysis, participated in the writing, reviewing, and editing the different states of the manuscript. J.K. oversaw the development of the project, obtained funding and resources, designed the clinical protocol, carried out formal analysis, and developed mathematical, statistical and computational analyses. M.E.M.R. participated in the writing reviewing and editing of the manuscript at different stages, pre and post publication. G.G.G in charge of data curation. L.I.V.G.L. designed the methodology, carried out experiments collected data and evidence. G.C.L.A. conceptualization of the project's objectives and goals, designed the methodology, carried out statistical analyses oversaw the general project, participated in the writing of the initial manuscript, carried out and participated in the translation to English language. All authors reviewed and approved the final version of the manuscript.

## REFERENCES

- [1] Curlin M, Bursac D. Cervical mucus from biochemical structure to clinical implications. *Front Biosci (Schol Ed)* [Internet]. 2013;5(2):507-515. Available from: <https://doi.org/10.2741/S386>
- [2] Daunter B, Counsilman C. Cervical mucus: Its structure and possible biological functions. *Europ J Obstet Gynecol Reprod Biol* [Internet]. 1980;10(3):141-161. Available from: [https://doi.org/10.1016/0028-2243\(80\)90056-8](https://doi.org/10.1016/0028-2243(80)90056-8)
- [3] Nicosia SV. Physiology of Cervical Mucus Productionle. *Semin Reprod Med* [Internet]. 1986;4(4):313-321. Available from: <https://www.thieme-connect.de/products/ejournals/abstract/10.1055/s-2007-1022511>
- [4] Dubey V, Mythirayee S, Tiwari RK, Gaharwar U, et al. Cervical Mucus Helps in the Fertilization. *World J Pharm Pharm Sci* [Internet]. 2016;5(10):242-250 Available from: [https://www.researchgate.net/publication/316681786\\_CERVICAL\\_MUCUS\\_HELPS\\_IN\\_THE\\_FERTILIZATION](https://www.researchgate.net/publication/316681786_CERVICAL_MUCUS_HELPS_IN_THE_FERTILIZATION)
- [5] Nakano FY, Leão R de BF, Esteves SC. Insights into the role of cervical mucus and vaginal pH in unexplained infertility. *MedicalExpress* [Internet]. 2015;2(2): 1-8. Available from: <https://www.scielo.br/j/medical/a/qjRg5mV765Dvs5tYjCtBwyC/?form at=pdf&lang=en>
- [6] Fehring RJ. Accuracy of the peak day of cervical mucus as a biological marker of fertility. *Contraception* [Internet]. 2002;66(4):231-235. Available from: [https://doi.org/10.1016/S0010-7824\(02\)00355-4](https://doi.org/10.1016/S0010-7824(02)00355-4)
- [7] Murcia-Lora JM, Esparza-Encina ML. The Fertile Window and Biomarkers: A Review and Analysis of Normal Ovulation Cycles. *Pers Bioet* [Internet]. 2011;15(2):149-165. Available from: [http://www.scielo.org.co/scielo.php?script=sci\\_arttext&pid=S0123-31222011000200004&lng=en](http://www.scielo.org.co/scielo.php?script=sci_arttext&pid=S0123-31222011000200004&lng=en)
- [8] Abbara A, Vuong LN, Ho VNA, Clarke SA, et al. Follicle Size on Day of Trigger Most Likely to Yield a Mature Oocyte. *Front Endocrinol* [Internet]. 2018;9:193. Available from: <https://doi.org/10.3389/fendo.2018.00193>
- [9] Randviir EP, Banks CE. Electrochemical impedance spectroscopy: An overview of bioanalytical applications. *Anal Methods* [Internet]. 2013;5:1098-1115. Available from: <https://doi.org/10.1039/C3AY26476A>
- [10] Řezáč P. Potential applications of electrical impedance techniques in female mammalian reproduction. *Theriogenology* [Internet]. 2008;70(1):1-14. Available from: <https://doi.org/10.1016/j.theriogenology.2008.03.001>
- [11] Walker DC, Brown BH, Smallwood RH, Hose DR, et al. Modelled current distribution in cervical squamous tissue. *Physiol Meas* [Internet]. 2002;23(1):159. Available from: <https://doi.org/10.1088/0967-3334/23/1/315>
- [12] Albrecht BH, Fernando RS, Regas J, Betz G, et al. A new method for predicting and confirming ovulation. *Fertil Steril* [Internet]. 1985;44(2):200-205. Available from: [https://doi.org/10.1016/S0015-0282\(16\)48736-4](https://doi.org/10.1016/S0015-0282(16)48736-4)
- [13] Moreno JE, Khan-Dawood FS, Goldzieher JW. Natural family planning: Suitability of the CUETM method for defining the time of ovulation. *Contraception* [Internet]. 1997;55(4):233-237. Available from: [https://doi.org/10.1016/S0010-7824\(97\)00007-3](https://doi.org/10.1016/S0010-7824(97)00007-3)
- [14] Moreno JE, Weitzman GA, Doody MC, Gibbons WE, et al. Temporal relation of ovulation to salivary and vaginal electrical resistance patterns: Implications for natural family planning. *Contraception* [Internet]. 1988;38(4):407-418. Available from: [https://doi.org/10.1016/0010-7824\(88\)90082-0](https://doi.org/10.1016/0010-7824(88)90082-0)
- [15] Brown BH, Milnes P, Abdul S, Tidy JA. Detection of cervical intraepithelial neoplasia using impedance spectroscopy: A prospective study. *BJOG* [Internet]. 2005;112(6):802-806. Available from: <https://doi.org/10.1111/j.1471-0528.2004.00530.x>
- [16] Brown BH, Tidy JA, Boston K, Blackett A, et al. Relation between tissue structure and imposed electrical current flow in cervical neoplasia. *Lancet* [Internet]. 2000;355(9207):892-895. Available from: [https://doi.org/10.1016/S0140-6736\(99\)09095-9](https://doi.org/10.1016/S0140-6736(99)09095-9)
- [17] Gandhi SV, Walker DC, Brown BH, Anumba DO. Comparison of human uterine cervical electrical impedance measurements derived using two tetrapolar probes of different sizes. *Biomed Eng Online* [Internet]. 2006;5:62. Available from: <https://doi.org/10.1186/1475-925X-5-62>
- [18] Gandhi SV, Walker D, Milnes P, Mukherjee S, et al. Electrical impedance spectroscopy of the cervix in non-pregnant and pregnant women. *Eur J Obstet Gynecol Reprod Biol* [Internet]. 2006;129(2):145-149. Available from: <https://doi.org/10.1016/j.ejogrb.2005.12.029>
- [19] Jokhi RP, Ghule VV, Brown BH, Anumba DO. Reproducibility and repeatability of measuring the electrical impedance of the pregnant human cervix-the effect of probe size and applied pressure. *Biomed Eng Online* [Internet]. 2009;8:10. Available from: <https://doi.org/10.1186/1475-925X-8-10>
- [20] Saito TK de S, Pedriali RA, Gabella CM, Chaves Junior M, et al. Preliminary results of cervical impedance measurements. *Res Biomed Eng* [Internet]. 2018;34(02):110-114. Available from: <https://doi.org/10.1590/2446-4740.05617>
- [21] Timing of ovulation based on vaginal pH by Gorodeski GI, Liu CC. (2008, Mar. 20). Patent 11/574279 [Internet]. Available from: <https://uspto.report/patent/app/20080071190>
- [22] Freundl G, Bremme M, Frank-Herrmann P, Godehardt E, et al. The CUE fertility monitor compared to ultrasound and LH peak measurements for fertile time ovulation detection. *Adv Contracept* [Internet]. 1996;12:111-121. Available from: <https://doi.org/10.1007/BF01849632>
- [23] Vigil P, Cortés ME, Carrera B, Hauyón R, et al. El moco cervical en la fisiología reproductiva. In: Guzmán E, Croxatto H, Lalonde A (eds). *Cervical Mucus in Human Reproduction*. Copenhagen: Scriptor; 2014. 325-334p.
- [24] Faes TJC, van der Meij HA, de Munck JC, Heethaar RM. The electric resistivity of human tissues (100 Hz-10 MHz): a meta-analysis of review studies. *Physiol Meas* [Internet]. 1999;20:R1. Available from: <https://doi.org/10.1088/0967-3334/20/4/201>
- [25] Gould KG, Ansari AH. Electrolyte interactions in cervical mucus and their relationship to circulating hormone levels. *Contraception*. 1981; Available from: [https://doi.org/10.1016/0010-7824\(81\)90078-0](https://doi.org/10.1016/0010-7824(81)90078-0)

[dx.doi.org/10.17488/RMIB.43.3.2](https://dx.doi.org/10.17488/RMIB.43.3.2)

E-LOCATION ID: 1280

## Segmentation of OCT and OCT-A Images using Convolutional Neural Networks

### Segmentación de imágenes de OCT y OCT-A por medio de Redes Neuronales Convolucionales

Fernanda Cisneros-Guzmán , Manuel Toledano-Ayala , Saúl Tovar-Arriaga  , Edgar A. Rivas-Araiza 

Universidad Autónoma de Querétaro - México

#### ABSTRACT

Segmentation is vital in Optical Coherence Tomography Angiography (OCT-A) images. The separation and distinction of the different parts that build the macula simplify the subsequent detection of observable patterns/illnesses in the retina. In this work, we carried out multi-class image segmentation where the best characteristics are highlighted in the appropriate plexuses by comparing different neural network architectures, including U-Net, ResU-Net, and FCN. We focus on two critical zones: retinal vasculature (RV) and foveal avascular zone (FAZ). The precision obtained from the RV and FAZ segmentation over 316 OCT-A images from the OCT-A 500 database at 93.21% and 92.59%, where the FAZ was segmented with an accuracy of 99.83% for binary classification.

**KEYWORDS:** OCT-A segmentation, ResU-Net, FCN segmentation, Convolutional Neural Network

## RESUMEN

La segmentación juega un papel vital en las imágenes de angiografía por tomografía de coherencia óptica (OCT-A), ya que la separación y distinción de las diferentes partes que forman la mácula simplifican la detección posterior de patrones/enfermedades observables en la retina. En este trabajo, llevamos a cabo una segmentación de imágenes multiclase donde se destacan las mejores características en los plexos apropiados al comparar diferentes arquitecturas de redes neuronales, incluidas U-Net, ResU-Net y FCN. Nos centramos en dos zonas críticas: la segmentación de la vasculatura retiniana (RV) y la zona avascular foveal (FAZ). La precisión para RV y FAZ en 316 imágenes OCT-A de la base de datos OCT-A 500 se obtuvo en 93.21 % y 92.59 %. Cuando se segmentó la FAZ en una clasificación binaria, con un 99.83% de precisión.

**PALABRAS CLAVE:** Segmentación OCT-A, ResU-Net, segmentación FCN, Red neuronal convolucional

### Corresponding author

TO: Saúl Tovar Arriaga

INSTITUTION: Universidad Autónoma de Querétaro

ADDRESS: Cerro de las Campanas S/N,

Col. Las Campanas, C. P. 76010, Santiago de Querétaro, Querétaro, México

CORREO ELECTRÓNICO: saul.tovar@uaq.mx

### Received:

25 May 2022

### Accepted:

31 August 2022



## INTRODUCTION

The retina is located at the back of the eye and is a light-sensitive layer of tissue; its characteristic color is reddish or orange due to the number of blood vessels behind it. The macula is the yellowish area of the retina where vision is most affected and consists of the fovea, which is only a tiny part of the retina but is crucial to enable many visual functions, and by the foveal avascular zone (FAZ), the which allows the human being to detect light without dispersion or loss <sup>[1]</sup>.

Optical coherence tomography (OCT) is an imaging technique with micrometer resolution, which captures two-dimensional and three-dimensional images using low-coherence light from optical scattering media. The output images allow information about the retina, such as its structure, consistency, and thickness. It allows the diagnosis, monitoring, and control of retinal diseases through high-resolution images.

Optical coherence tomography angiography (OCT-A) is a modern, non-invasive technology that, like OCT, allows retina imaging. The main advantage of OCT-A is that it does not require the application of a contrast agent to obtain deep and superficial images of the retinal blood vessels (RV). The FAZ is a central nonvascular area. Previous studies can obtain the images of the projection maps (superficial, internal, and deep). It is necessary to point out that each plexus has different morphological characteristics; therefore, they are visualized both on the surface and in the internal plexus <sup>[2]</sup>.

In this article, a comparison between the plexus segmentation taken with different imaging modalities, namely OCT and OCT-A, is first presented to identify which of the two imaging techniques offers the best conditions for segmentation. The main characteristics of the plexus are the ZAF and the RV. Once the best modality has been identified, we will only take the copies of it to carry out the segmentation correspond-

ing to the characteristics sought. For the FAZ, a comparison between two convolutional networks, U-Net and ResU-Net, is used, and for the RV characteristic, a Fully Convolutional Network (FCN) and U-Net. Both factors differ in one of the networks to be compared because the FCN has presented better results in terms of detail at the edges of the characteristics sought to be segmented.

## Related Work

The semantic segmentation task is one of the essential tasks in computer vision in recent decades and even more so if we focus on medical images since they have become an aid in detecting diseases. It has been proven that using neural networks to perform this task yields good results. However, when we talk about semantic segmentation, it is prevalent that convolutional networks are used from start to finish.

The development of these networks for medical images has been used in countless applications, whether in the eyes, chest, abdomen, brain, or heart. The database used for this article is from the retina, that is, from the human eye. Therefore, we will contribute with state of the art of retina analysis. One of the challenges is the segmentation of veins or blood vessels. It depends on the technique to obtain an image, such as an eye fundus image or a tomography taken to some specific area. In <sup>[3]</sup> <sup>[4]</sup>, use a residual network based on U-Net using a batch normalization and an automatic encoder named PixelBNN, which segments the veins in fundus images and is tested in various databases to achieve acceptable results; down testing time was their contribution. For Xiao *et al.* and Son J *et al.*, the contribution to RV focused on reducing the edges of the veins, making them more precise and sharper <sup>[5]</sup> <sup>[6]</sup>. Other ocular applications in the area of glaucoma where the main task is to segment the optic disc, in <sup>[7]</sup> <sup>[8]</sup> use a ResU-Net and propose using a modified FCN; the image takes to center in the optic disk to reduce noise in fundus images.

## RV segmentation

OCT-A is a non-invasive technique developed and applied relatively a few years ago, through which the vascular structures and choroids can be visualized in the retina. In turn, the segmentation of retinal vessels, the obtained vasculature through this technique, is an available research opportunity to make a difference from the methods studied for more than 20 years<sup>[9] [10] [11]</sup>, such as those based on techniques such as deep learning, filters, and some classifiers for VR segmentation in fundus images. Implemented the method used in image thresholding in<sup>[4] [5]</sup> to determine the density of the veins.

However, vector and exponential flow optimization algorithms have been among the best algorithms implemented in OCTA images for RV enhancement and segmentation. The implementation based on Gibbs Markov and its field model in<sup>[12] [13] [14]</sup> was applied in the projection maps for the RV segmentation to segment retinal vessels into different projection maps.

The papers of<sup>[8] [9] [10]</sup> proposed a modified U-Net for circle segmentation in a maximum intensity projection of OCT-A. Wylęgała *et al.* present in<sup>[11]</sup> a new partition-based modular array to detect thick and thin vessels separately.

## FAZ segmentation

The FAZ is the fovea region where the absence of blood, the vasculature, can be observed. A new field of study is the segmentation of the FAZ through OCT-A images compared to retinal vascular segmentation. The authors of the papers<sup>[12] [13] [14]</sup> introduced an active contour model for FAZ detection. Li *et al.* and Bates *et al.* present in<sup>[15] [16]</sup> a series of morphological factors to identify FAZ candidates in OCTA projections using two types of fields of view. A modified U-Net to segment the FAZ on the OCTA projection map of the superficial retina was introduced in the papers<sup>[9] [16]</sup>. Through a CNN, Azzopardi *et al.* develops a segmentation for the FAZ and the nonischemic capillary region<sup>[12]</sup>.

## MATERIALS AND METHODS

### Dataset

The plexuses database deployed in this work is the OCTA-500<sup>[15]</sup>, which consists of images collected from 500 subjects taken under identical conditions (projection maps). The retina image size is 3mm x 3mm, with 304px by 304px collected from 200 subjects, and 6mm x 6mm images, with 400px by 400px for the remaining 300 subjects. Images with the same number and characteristics were collected for OCT and OCT-A.

Figure 1 shows the OCT and OCT-A projection maps from the OCTA-500 database. The corresponding OCT projections and the full OCT-A projection correspond to 3D volumes from averaging in the axial direction. On the other hand, the Inner Limiting Membrane (ILM) - Outer Plexiform Layer (OPL) projections, as well as the OPL - Brunch Membrane (BM), respond to a maximum in the same direction.

### U-Net

U-Net is a network based on a "Fully Convolutional Network" (FCN) which was designed, tested, and presented in 2015 mainly for the segmentation of biomedical images. The value and reliability that U-Net offers, with its 23 convolutional layers, has been shown in<sup>[17]</sup> for the field of images of medical origin. A network that does not entirely connect all its layers and when taking the shape of a "U" reflects almost a symmetry in the expansive and contraction paths.

Due to the nature of the network in this article, it was decided to use the same architecture proposed in<sup>[17]</sup><sup>[18]</sup>, which can be defined in general terms as a network formed by a series of encoders located in the first half of the network, which allows the data to be contextualized, input is called the contraction path. This first part of the network is built from unpadded convolutions, followed by a rectified linear unit activation layer ReLU<sup>[19]</sup> for each previous convolution.

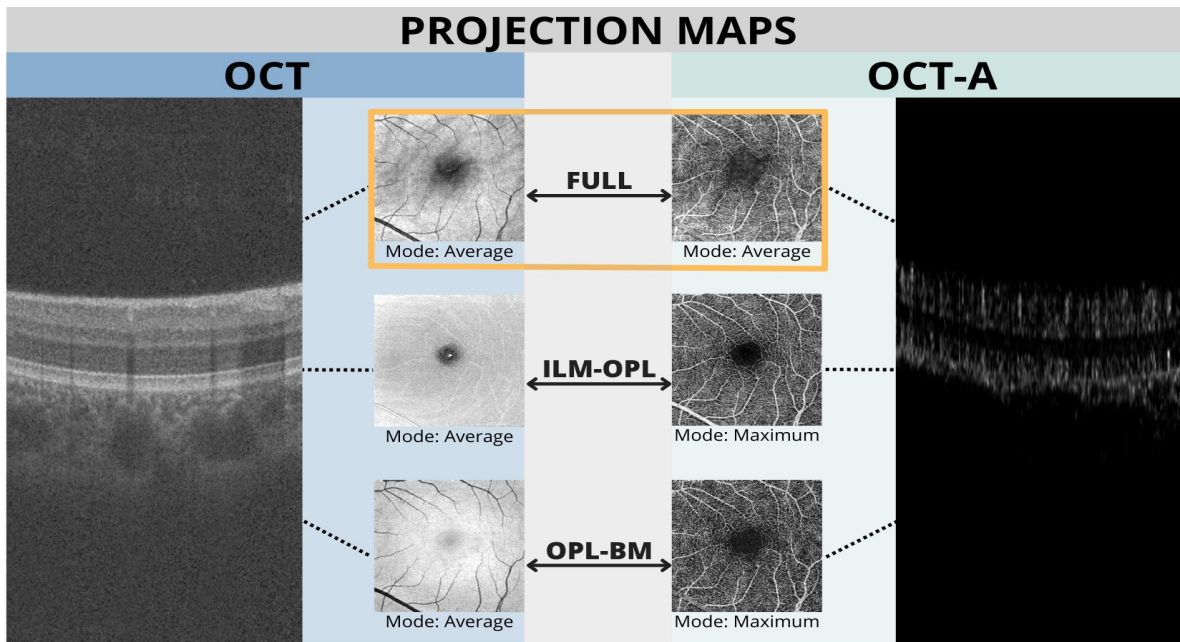


FIGURE 1. Projection maps for each of the techniques (All images are retrieved from the database <sup>[15]</sup>)

Finally, the resolution reduction applies a maximum grouping operation. In the second half, the expansion path, a series of decoders perform the exact location of the network by determining it from an upsampling of the function map, followed by an up-convolution, cropping, and two convolutions that, like in the first half it is followed by a ReLU layer for each of them.

### Deep ResU-Net

ResU-Net is a semantic segmentation neural network that merges the strengths of the residual neural networks and the U-Net, thus obtaining a Deep ResU-Net. This combination provides two advantages: 1) the residue facilitates the formation of meshes; 2) it facilitates the lossless transmission of information between the low and high levels of the network and within a residual unit with the elimination of connections, which allows for designing a neural network with fewer parameters <sup>[20] [21]</sup>. It can achieve similar performance and is consistently better than semantic segmentation.

The architecture of the ResU-Net network comprises 56 convolutional layers; the network proposal by <sup>[20]</sup> solves the degradation of the model in the deeper layers.

A model builds to the base of the pair of convolutional layers corresponding to the expansive path in the U-Net; a residual learning block replaces these. A residual learning block comprises three convolutional layers, the first two with a ReLU activation and three batch normalization layers <sup>[21]</sup>. Hence the ResU-Net on the expansive path includes an input unit, a central unit, and a residual unit; the contraction path comprises four concatenated blocks, adding a block and an output unit.

### Fully Convolutional Network

A Fully Convolutional Network (FCN) can be used for semantic segmentation, which means it uses convolution and deconvolution layers. For the development of this research, a FCN network was developed and tested by <sup>[22]</sup> based on a VVG-16 as the authors mention higher accuracy compared to other FCN based on either AlexNet or GoogLeNet. Three variations are known for the FCN network, FCN8s, FCN16s, and FCN32s; in our case, a FCN8s network is used. The discrepancy between these three networks lies in the resolution reduction because the semantic information requires a detailed level of recovery in the connection of the intermediate layers.

## Evaluation Metrics

It is essential to mention that due to the nature of the problem in the segmentation of both the FAZ and the RV, the background of the image has a more significant presence than each of the parts to be segmented. Therefore, the metrics <sup>[23]</sup> chosen to evaluate the segmentation performance of each network quantitatively are established in equations (1) - (5):

- Dice Coefficient (DICE):

$$\frac{2TP}{(2TP + FP + FN)} \quad (1)$$

- Jaccard index (JAC):

$$\frac{TP}{(TP + FP + FN)} \quad (2)$$

- Balance-precision (BACC):

$$TPR + TNR \quad (3)$$

- Precision (PRE):

$$\frac{TP}{(TP + FP)} \quad (4)$$

- Recovery (REC):

$$\frac{TP}{(TP + FN)} \quad (5)$$

These metrics allow comparing our models with the current state-of-the-art. TPR refers to the true positive rate, TNR negative rate, TP to True Positive, and FN to False Negative.

## Manual Segmentation

The ground truth (GT) used to validate the results of the following training sessions is one for each feature.

The ground truth (GT) used to validate the results differs from the given to the database. A manual modification is made to the image provided where the features are isolated, and the original GT has both features FAZ and RV. Figure 2 shows the segmentation of the FAZ; the GT is unique for this feature, doing away with the RV and only placing a black background in the rest of the image. This same process is carried out for the GT of the RV.

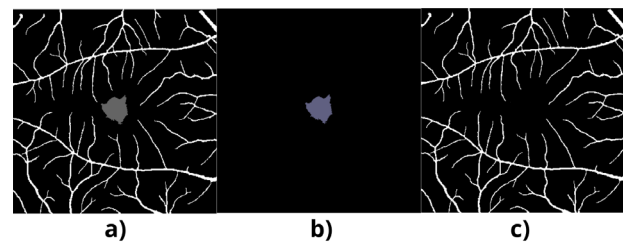


FIGURE 2. a) GT OCTA-500; b) GT of FAZ; c) GT of RV.

## Process

Model training is performed using 80% of the images from the full projection, which correspond to 400 photos from the OCTA-500 database, and the remaining 20% was used for verification. Resizing 304 px by 304 px is applied for the test and training set to keep data in standard dimensions. This procedure is performed under the same conditions and characteristics of retinal imaging.

It uses the U-Net network while preserving the structure and hyperparameters of the original model using the Stochastic Gradient Optimizer (SGD). The training is performed for 50 epochs for both databases. Figure 3 shows the evolution of the proposed methodology in detail.

Additional training is carried out with a technique that performs a better segmentation of the validation image and compares it with the ground truth, provided and validated by the same database used (OCTA-500). OCT-A technology provides the best measurements; however, the goal was to segment the FAZ, and

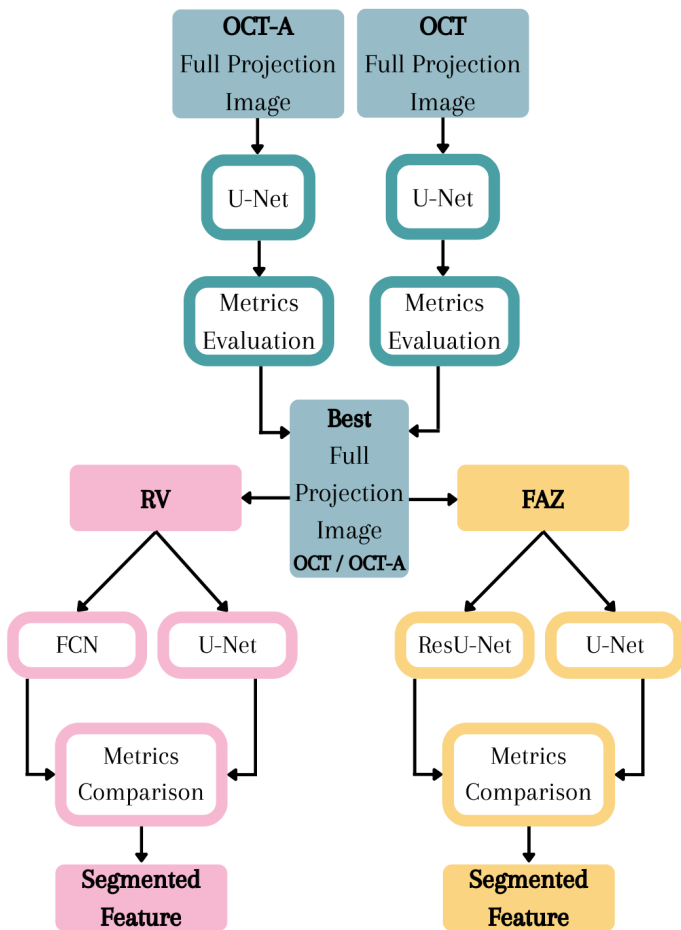


FIGURE 3. Metodology.

in the results, blood vessels can be observed in the full segmented view of both techniques. In addition, manual segmentation was performed in the target image to enhance the above segmentation, leaving only the visible FAZ, ignoring the vascular system. It is important to note that this training is conducted under conditions similar to those previously applied.

Two projection maps from the database were mainly used for RV segmentation. One of them is the maximum projection map of the retina and the full projection map. These two maps can be found for the two imaging techniques, that is, OCT and OCT-A, which allows a more significant number of examples for training.

### Technical Considerations

All experimentation is done in TensorFlow using an NVIDIA GeForce GTX 1080Ti GPU. The standard normal initialization method is used to initialize the network with a difference of 0.02 batch size of 3 as a cross-entropy loss function, and Adam as the optimizer was implemented.

Overtraining is avoided by evaluating the similarity between the validation and training sets throughout the network training process. Further choosing the training model with the best performance and trying to have the best value of this similarity by calculating the dice coefficient.

### RESULTS AND DISCUSSION

It is observed that the OCT image produced poor segmentation compared to the OCT-A image. It is essential to point out that this segmentation is not acceptable because the distinction between the FAZ and the veins cannot be differentiated in the image; only an image with a black background and some white reliefs are observed. In Figure 4, we support this, and the applied metrics are presented after a comparison.

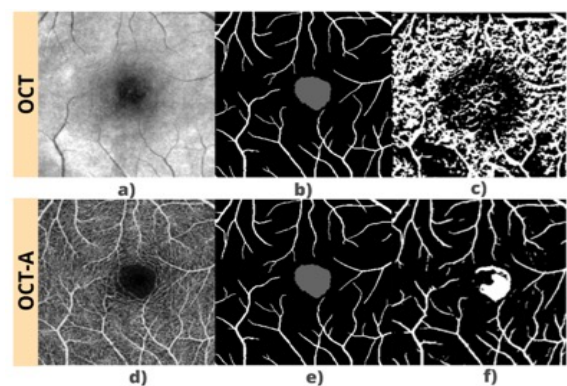


FIGURE 4. Resulting Image. OCT: a) Full projection, b) Ground Truth, c) U-Net-FAZ. OCT-A: d) Full projection, e) Ground Truth, f) U-Net-FAZ.

In the case of OCT, in a visual evaluation of Figure 4, it is impossible to locate the FAZ or the veins in the resulting image (c). Despite showing an accuracy of

88.42%, there is no correct segmentation. High precision in the OCT images is due to the nature of the images; that is, we can see that the validation image (b) has a black background, which is why it shows an acceptable precision when evaluating. In the case of OCT-A, in the resulting image (c), it is possible to visualize the two elements of interest, the FAZ, and the veins. Even though errors are shown in the segmentation in said segmentation, the clarity is apparent in the image, and it is evident.

Table 1 and Figure 5 compare the network implementation of two data sets prepared in the same condition. As we can see, OCT-A retinal imaging presents better results.

**TABLE 1. Validation Metrics.**

Metric	OCT	OCT-A
Loss	0.3164	0.1627
Accuracy	88.42%	97.77%
AUC	87.71%	92.04%

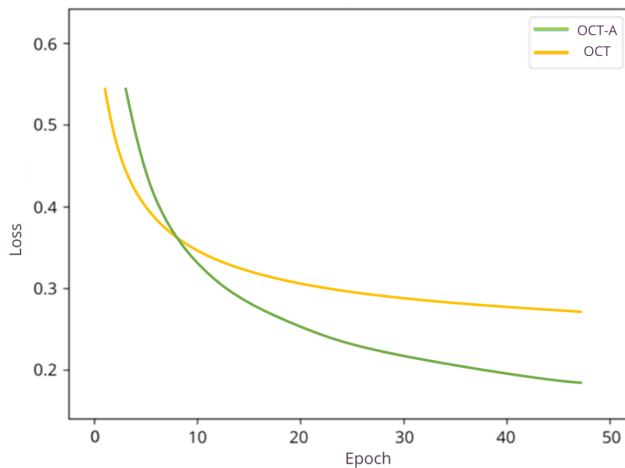


**FIGURE 5. Comparison of the loss OCT vs. OCT-A6.**

Earlier mentioned, a second training cycle (Table 2) was applied to this technique. The main change is that the mask does not contain vessels (only the FAZ), our area of interest.

**TABLE 2. Validation Training-Second Training.**

Metric	OCT-A
Loss	0.1194
Accuracy	99.83%
AUC	98.74%

Tested this second training and the architectures, the results show us that in the case of the FAZ, the metrics validate that the best segmentation was through training with the ResU-Net network. Furthermore, visual assessment (Figure 6) is confirmation that the feature is fully segmented.

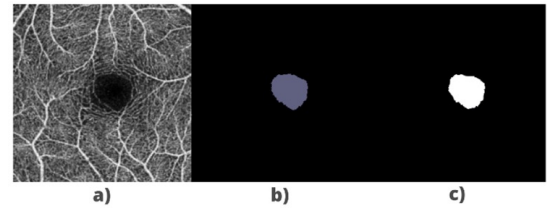


**FIGURE 6. FAZ ResU-Net Segmentation: a) Original image; b) Grand Truth; c) Segmentation obtained.**

Furthermore, the performance obtained from the networks in the validation data is shown in Table 3. The ResU-Net network is observed to be better than the U-Net under the abovementioned metrics.

**TABLE 3. Metrics comparison of different methods for FAZ segmentation.**

Issue	Method	DICE (%)	JAC (%)	BACC (%)	PRE (%)	REC (%)
FAZ	U-Net	85.18	76.43	92.65	88.07	85.44
	ResU-Net	89.99	89.36	93.63	92.59	93.61

On the other hand, for the veins, the network that gives the best results after the training is the FCN shown in Figure 7, where it is possible to observe in the

same way as in the case of the FAZ. In this isolated segmentation, the mask (GT) only shows the blood vessels, and the result of this change gives a segmentation with the distinction of the veins in the image.

Figure 7 and Table 4 correspond to the RV feature, and we can observe and confirm that the FCN segmentation is the have the best metrics and is also affirmed under the visual test segmentation.

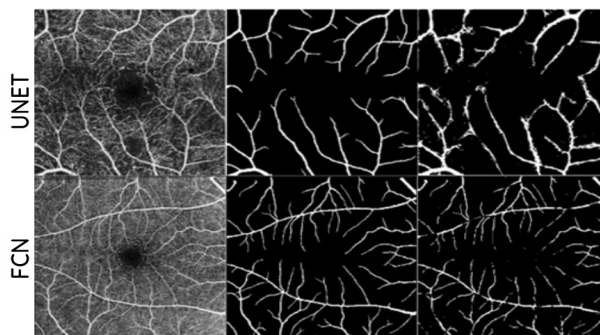


**FIGURE 7. Retina comparison of blood vessel segmentation.**

**TABLE 4. Metrics comparison of different methods for RV segmentation.**

Issue	Method	DICE (%)	JAC (%)	BACC (%)	PRE (%)	REC (%)
RV	U-Net	80.43	70.75	88.70	91.35	82.96
	ResU-Net	86.26	78.26	91.78	93.21	86.57

## CONCLUSIONS

According to our segmentation results, it was better to implement a DL model separately for each characteristic. This may be because the characteristics differ a lot from each other. For each neural network, RV segmentation and FAZ segmentation were implemented separately. Manual segmentation was performed on the ground truth (GT) images. Using GT images with isolated segmentation allows the network to perform validation that only focuses on the desired feature. We compare state-of-the-art segmentation methods, including U-Net, ResU-Net, and FCN, for the FAZ segmentation. ResU-Net gives us a similarity percentage with the actual segmentation image of almost 90%. As for the RVs, the similarity is close to 86% using the FCN network. The obtained results are satisfactory enough to be used in the application or detection of these patterns for disease detection.

## AUTHOR CONTRIBUTION

M.F.C.G. conceptualized the project, collected, gathered and curated data, designed and developed the methodology and modelling, participated in the design of software, and in the writing of the manuscript. S.T.A. conceptualized the project, curated data and designed and developed the methodology and modelling, wrote original draft. M.T.A. conceptualized the project, reviewed, and edited final version of the manuscript. E.A.R.A. reviewed and edited final version of the manuscript. All authors reviewed and approved the final version of the manuscript.

## REFERENCES

- [1] Wons J, Pfau M, Wirth MA, Freiberg FJ, et al. Optical coherence tomography angiography of the foveal avascular zone in retinal vein occlusion. *Ophthalmologica* [Internet]. 2016; 235:195-202. Available from: <https://doi.org/10.1159/000445482>
- [2] Guo M, Zhao M, Cheong AMY, Dai H, et al. Automatic quantification of superficial foveal avascular zone in optical coherence tomography angiography implemented with deep learning. *Vis Comput Ind Biomed Art* [Internet]. 2019;2:21. Available from: <https://doi.org/10.1186/s42492-019-0031-8>
- [3] Leopold HA, Orchard J, Zelek JS, Lakshminarayanan V. PixelBNN: Augmenting the Pixelcnn with Batch Normalization and the Presentation of a Fast Architecture for Retinal Vessel Segmentation. *J Imaging* [Internet]. 2019;5(2):26. Available from: <https://doi.org/10.3390/jimaging5020026>
- [4] Zhang Y, Chung ACS. Deep Supervision with Additional Labels for Retinal Vessel Segmentation Task. In: Frangi A, Schnabel J, Davatzikos C, Alberola-López C, et al. (eds). *Medical Image Computing and Computer Assisted Intervention - MICCAI 2018* [Internet]. Granada, Spain: Springer; 2018:83-91. Available from: [https://doi.org/10.1007/978-3-030-00934-2\\_10](https://doi.org/10.1007/978-3-030-00934-2_10)
- [5] Xiao X, Lian S, Luo Z, Li S. Weighted Res-UNet for High-Quality Retina Vessel Segmentation. In: 2018 9th International Conference on Information Technology in Medicine and Education (ITME) [Internet]. Hangzhou, China: IEEE; 2018: 327-331. Available from: <https://doi.org/10.1109/ITME.2018.00080>
- [6] Son J, Park SJ, Jung KH. Towards Accurate Segmentation of Retinal Vessels and the Optic Disc in Fundoscopic Images with Generative Adversarial Networks. *J Digit Imaging* [Internet]. 2019;32(3):499-512. Available from: <https://doi.org/10.1007/s10278-018-0126-3>
- [7] Jayabalan GS, Bille JF. The Development of Adaptive Optics and Its Application in Ophthalmology. In: Bille J. (eds). *High Resolution Imaging in Microscopy and Ophthalmology* [Internet]. Cham, Switzerland: Springer; 2019: 339-358p. Available from: [https://doi.org/10.1007/978-3-030-16638-0\\_16](https://doi.org/10.1007/978-3-030-16638-0_16)
- [8] Taher F, Kandil H, Mahmoud H, Mahmoud A, et al. A Comprehensive Review of Retinal Vascular and Optical Nerve Diseases Based on Optical Coherence Tomography Angiography. *Appl Sci* [Internet]. 2021;11(9):4158. Available from: <https://doi.org/10.3390/app11094158>
- [9] Spaide RF, Fujimoto JG, Waheed NK, Sadda SR, et al. Optical coherence tomography angiography. Vol. 64, *Prog Retin Eye Res* [Internet]. 2018;64:1-55. Available from: <https://doi.org/10.1016/j.preteyeres.2017.11.003>
- [10] de Carlo TE, Romano A, Waheed NK, Duker JS. A review of optical coherence tomography angiography (OCTA). *Int J Retin Vitre* [Internet]. 2015;1:5. Available from: <https://doi.org/10.1186/s40942-015-0005-8>
- [11] Wylegała A, Teper S, Dobrowolski D, Wylegała E. Optical coherence angiography: A review. *Medicine* [Internet]. 2016;95(41):e4907. Available from: <https://doi.org/10.1097/MD.0000000000004907>
- [12] Azzopardi G, Strisciuglio N, Vento M, Petkov N. Trainable COSFIRE filters for vessel delineation with application to retinal images. *Med Image Anal* [Internet]. 2015;19(1):46-57. Available from: <https://doi.org/10.1016/j.media.2014.08.002>
- [13] Lau QP, Lee L, Hsu W, Wong TY. Simultaneously Identifying All True Vessels from Segmented Retinal Images. *IEEE Trans Biomed Eng* [Internet]. 2013;60(7):1851-1858. Available from: <https://doi.org/10.1109/tbme.2013.2243447>
- [14] Ghazal M, Al Khalil Y, Alhalabi M, Fraiwan L, et al. 9-Early detection of diabetics using retinal OCT images. In: El-Baz AS, Suri JS (eds). *Diabetes and Retinopathy* [Internet]. United States: Elsevier; 2020. 173-204p. Available from: <https://doi.org/10.1016/B978-0-12-817438-8.00009-2>
- [15] Li W, Zhang Y, Ji Z, Xie K, et al. IPN-V2 and OCTA-500: Methodology and Dataset for Retinal Image Segmentation, distributed by Cornell University [Internet]. 2020. Available from: <https://doi.org/10.48550/arXiv.2012.07261>
- [16] Bates NM, Tian J, Smiddy WE, Lee W-H, et al. Relationship between the morphology of the foveal avascular zone, retinal structure, and macular circulation in patients with diabetes mellitus. *Sci Rep* [Internet]. 2018;8:5355. Available from: <https://doi.org/10.1038/s41598-018-23604-y>
- [17] Ronneberger O, Fischer P, Brox T. U-net: Convolutional Networks for Biomedical Image Segmentation. In: Navab N, Hornegger J, Wells W, Frangi A (eds). *Medical Image Computing and Computer-Assisted Intervention - MICCAI 2015* [Internet]. Munich, Germany: Springer; 2015: 234-241. Available from: [https://doi.org/10.1007/978-3-319-24574-4\\_28](https://doi.org/10.1007/978-3-319-24574-4_28)
- [18] Sappa LB, Okuwobi IP, Li M, Zhang Y, et al. RetFluidNet: Retinal Fluid Segmentation for SD-OCT Images Using Convolutional Neural Network. *J Digit Imaging* [Internet]. 2021;34(3):691-704. Available from: <https://doi.org/10.1007/s10278-021-00459-w>
- [19] Rasamoelina AD, Adjailia F, Sinčák P. A Review of Activation Function for Artificial Neural Network. In: 2020 IEEE 18th World Symposium on Applied Machine Intelligence and Informatics (SAMII) [Internet]. Herlany, Slovakia: IEEE; 2020: 281-286. Available from: <https://doi.org/10.1109/SAMI48414.2020.9108717>
- [20] Qi W, Wei M, Yang W, Xu C, et al. Automatic Mapping of Landslides by the ResU-Net. *Remote Sens* [Internet]. 2020;12(15):2487. Available from: <https://doi.org/10.3390/rs12152487>
- [21] Ioffe S, Szegedy C. Batch Normalization: Accelerating Deep Network Training by Reducing Internal Covariate Shift. In: *ICML'15: Proceedings of the 32nd International Conference on International Conference on Machine Learning - Volume 37* [Internet]. Lille, France: JMLR; 2015: 448-456. Available from: <https://dl.acm.org/doi/10.5555/3045118.3045167>
- [22] He Y, Carass A, Liu Y, Jedynek BM, et al. Fully Convolutional Boundary Regression for Retina OCT Segmentation. In: Shen D, Liu T, Peters TM, Staib LH, et al. (eds). *Medical Image Computing and Computer Assisted Intervention - MICCAI 2019*. MICCAI 2019 [Internet]. Shenzhen, China: Springer; 2019: 120-128. Available from: [https://doi.org/10.1007/978-3-030-32239-7\\_14](https://doi.org/10.1007/978-3-030-32239-7_14)
- [23] Liu X, Song L, Liu S, Zhang Y. A review of Deep-Learning-Based Medical Image Segmentation Methods. *Sustainability* [Internet]. 2021;13(3):1224. Available from: <https://doi.org/10.3390/su13031224>



[dx.doi.org/10.17488/RMIB.43.3.3](https://dx.doi.org/10.17488/RMIB.43.3.3)

E-LOCATION ID: 1298

## Electrical Impedance Tomography to Measure Spirometry Parameters in Chronic Obstructive Pulmonary Disease Patients

### Tomografía por Impedancia Eléctrica para Medir Parámetros de Espirometría en Pacientes con Enfermedad Pulmonar Obstructiva Crónica

Francisco Miguel Vargas Luna<sup>1</sup> , Svetlana Kashina<sup>1</sup> , Pere Joan Riu Costa<sup>2</sup> , Pere Casan Clarà<sup>3</sup> ,  
José Marco Balleza Ordaz<sup>1</sup>  

<sup>1</sup>División de Ciencias e Ingenierías, Universidad de Guanajuato, Campus León - Guanajuato, Mexico

<sup>2</sup>Universidad Politécnica de Cataluña - Barcelona, Spain

<sup>3</sup>Research Institute of the Principality of Asturias, ISPA, University of Oviedo - Oviedo, Spain

#### ABSTRACT

Spirometry is a test for the diagnosis of chronic obstructive pulmonary disease. It is a technique that can be intolerant due to the essential use of a mouthpiece and a clamp. This study proposes the use of electrical impedance tomography to measure respiratory parameters. Patients underwent spirometry and three respiratory exercises. The impedance signals were convolved, and the resultant was analyzed by fast Fourier transform. The frequency spectrum was divided into seven segments (R1 to R7). Each segment was represented in terms of quartiles (Q25%, Q50%, Q75%). Each quartile of each segment was correlated with the spirometric parameters to obtain a fitting equation. FVC was correlated 70% with the 3 quartiles of R7, 3 equations were obtained with a fit of 60%. FEV1 correlated 70% with the Q50% of R7, obtaining an equation with a fit of 40%. FEV1/FVC correlated 69% with Q75% of R2, obtaining an equation with a fit of 60%. Spirometric parameters can be estimated from the implied carrier frequency components of the ventilatory impedance signal.

**KEYWORDS:** Electrical impedance tomography, respiration, spirometry, calibration, monitoring

## RESUMEN

La espirometría es una prueba para el diagnóstico de enfermedad pulmonar obstructiva crónica. Es una técnica que puede resultar intolerante debido al uso imprescindible de una boquilla y una de pinza. Este estudio propone el uso de la tomografía de impedancia eléctrica para medir los parámetros respiratorios. Los pacientes realizaron una espirometría y tres ejercicios respiratorios. Las señales de impedancia fueron convolucionadas, y la resultante se analizó mediante una transformada rápida de Fourier. El espectro en frecuencias se dividió en siete segmentos (R1 a R7). Cada segmento se representó en términos de cuartiles (Q25%, Q50%, Q75%). Cada cuartil de cada segmento se correlacionó con los parámetros espirométricos para obtener una ecuación de ajuste. La FVC se correlacionó en un 70% con los 3 cuartiles de R7, se obtuvieron 3 ecuaciones con un ajuste del 60%. El FEV1 se correlacionó en un 70% con el Q50% de R7, obteniéndose una ecuación con un ajuste del 40%. El FEV1/FVC se correlacionó en un 69% con el Q75% de R2, obteniéndose una ecuación con un ajuste del 60%. Los parámetros espirométricos pueden ser estimados a partir de los componentes de frecuencia portadora implícitos de la señal de impedancia ventilatoria.

**PALABRAS CLAVE:** Tomografía por la impedancia eléctrica, respiración, espirometría, calibración, monitorización

### Corresponding author

TO: José Marco Balleza Ordaz

INSTITUTION: División de Ciencias e Ingenierías,  
Universidad de Guanajuato - Campus León

ADDRESS: Lomas del Bosque #103,

Col. Lomas del Campestre, C. P. 37150, León,  
Guanajuato, México

CORREO ELECTRÓNICO: [jm.balleza@ugto.mx](mailto:jm.balleza@ugto.mx)

### Received:

10 August 2022

### Accepted:

20 October 2022

## INTRODUCTION

Currently, mortality caused by chronic respiratory tract diseases is increasing in Mexico and occupied the fourth position in 2020. Chronic obstructive pulmonary disease (COPD) deaths are 2.49% of total mortality nationwide <sup>[1]</sup>. According to the Global Initiative for Chronic Obstructive Lung Disease, COPD showed a worldwide prevalence of 3.92% in 2017 (95% CI 3.52% - 4.32%). In 2021, the estimated global mortality rate was 42/100,000 (4.72%) and the DALY (Disability Adjusted Life Years) rate was 1068.02/100,000 inhabitants <sup>[2]</sup>. COPD is a common, preventable, and treatable disease characterized by persistent respiratory symptoms and airflow limitation due to airway and/or alveolar abnormalities, usually caused by significant exposure to noxious agents <sup>[2]</sup> <sup>[3]</sup>. The initial procedure for diagnosing COPD is spirometry, which is a non-invasive technique that measures the volume of air that the lungs can mobilize as a function of time <sup>[2]</sup> <sup>[3]</sup> <sup>[4]</sup>. However, the technique may be intolerant to the patient because of the use of a mouthpiece and nose clip, and the specific respiratory maneuver to be performed <sup>[5]</sup> <sup>[6]</sup> <sup>[7]</sup>.

Vogt *et al* <sup>[8]</sup> proposed the use of EIT to visualize the pulmonary ventilatory distribution (PVD) in a group of 35 COPD patients under the influence of an inhaled bronchodilator. Monitoring was performed immediately after inhalation and at 5, 10, and 20 minutes.

Signals from the EIT system and an electronic spirometer were recorded simultaneously. PVD was assessed by estimating the changes in impedance corresponding to the parameters: forced expiratory volume in 1 second (FEV<sub>1</sub>), forced vital capacity (FVC), pulmonary circulating volume (VC), peak flow (PF), and forced expiratory flow between 25 % and 75% of the FVC (FEF<sub>25-75%</sub>). The FEV<sub>1</sub>/FVC parameter was estimated from the elements of the EIT image to assess the post-bronchodilator effect in a regional manner. Only 17 showed a significant bronchodilator response. The FEV<sub>1</sub> parameter and CV changes showed

significant correlations with the impedance changes of the regions of interest of the EIT images in patients with bronchodilator response <sup>[8]</sup>.

Due to the above, this work proposes the use of the electrical impedance tomography (EIT) technique to measure the FVC, FEV<sub>1</sub>, and FEV<sub>1</sub>/FVC parameters from the respiratory recording obtained by EIT, analyzing the frequency components implicit in the changes in lung tidal volume. The objective of this study is to obtain a set of mathematical calibration models that adjust the module's frequency components powers (dB) and the phase of the impedance signal due to lung tidal volume obtained by EIT, to estimate the FVC, FEV<sub>1</sub>, and FEV<sub>1</sub>/FVC parameters.

## MATERIALS AND METHODS

### Pneumotachograph

Circulating volume measurements were obtained by a MedGraphics prevent TM Pneumotach kit (St. Paul, MN, USA). This system allows continuous recording of flow and time signals, both graphically and numerically. According to the standardized protocol, calibration was performed using a 3L syringe <sup>[9]</sup>.

### Electrical Impedance Tomography (EIT)

EIT was carried out with the TIE4sys system, experimental equipment designed by the Electronic Engineering Department of the Universitat Politècnica de Catalunya, Barcelona, Spain. The equipment uses 16 electrodes (Red Dot 2560 - 3 M, London, Ontario, Canada) placed around the chest, following the standardized protocol <sup>[10]</sup>. The calibration of the EIT system was performed on an arrangement of electrical resistance of 330 ohms as described in <sup>[11]</sup>. TIE4sys acquires 17 images/s and applies an alternating electrical current of 1 mA at 48 kHz through two adjacent electrodes. A differential voltage is detected across a pair of electrodes whose position is moved adjacently across the main 16-electrode array. Once the voltage

measurement cycle is finished, the injector pair moves to its adjacent position, starting a new measurement cycle. The measurement cycle ends when all electrodes have been used as current injectors and voltage detectors <sup>[11]</sup> <sup>[12]</sup>. EIT images are obtained using a weighted back-projection reconstruction algorithm. The EIT images are referential, a reference image is used to obtain subsequent images. This is reconstructed by obtaining and averaging 200 images corresponding to a lapse of 12 seconds of breathing <sup>[13]</sup>.

### Participants

A group of 15 patients diagnosed with COPD was analyzed. A spirometry test was performed and forced vital capacity (FVC), forced expiratory volume in 1 second (FEV1), and the ratio of the above parameters (FEV1/FVC) was also recorded. The examinations were carried out between 9:00 a.m. and 12:00 p.m. in a room with an ambient temperature of 25°C, 60% humidity, and at sea level. All of them voluntarily agreed to participate in the study, which had been previously approved by the center's Ethics Committee (Comité de Ética de la Secretaría de Salud del Estado de Guanajuato, México, del Hospital General de León, Approval Folio Number: GTSSA002101-364).

### Procedure

The pneumotachometer and the TIE4sys were simultaneously connected to each participant. Changes in the participants' circulating volume were recorded over 30 s, with a 3-min break between measurements. The number of cycles recorded for each individual varied between 20 and 25. For each respiratory exercise, 510 impedance measurements were recorded. In this study, three respiratory maneuvers per patient were acquired.

The data were analyzed and processed using the Python computer program <sup>[14]</sup>. A convolution of the three respiratory signals was performed <sup>[15]</sup>. In this case, the product of the first two signals was obtained

and the resulting signal was convolved with the third, obtaining the analysis signal. Subsequently, the resulting signal was analyzed by applying the Fast Fourier Transform (FFT). FFT is a mathematical process that transforms any time-varying signal into a frequency spectrum (FS) <sup>[16]</sup>. The FS was reconstructed with 182 data, dividing it into seven segments (from R1 to R7), each with 26 data, the minimum statistically significant amount to be analyzed independently. Segment R1 was defined between 0-117.49mHz, R2 between 156.66mHz-274.15mHz, R3 between 313.32mHz-430.18mHz, R4 between 469.98mHz-587.47mHz, R5 between 626.64mHz-744.13mHz, R6 between 783.30mHz-900. mHz and R7 between 939.95mHz-1.06Hz. The area under the curve (AuC) was estimated for each segment. The AuC is used to normalize the estimates of means or quartiles of each segment.

### Statistical analysis

The normal distribution of the data of each frequency segment was analyzed using the Shapiro-Wilk statistical test (S-W, significance value  $p < 0.05$ ). The correlation between the means and the FVC, FEV1, and FVC/FEV1 parameters was performed using the Pearson statistical test, establishing a significance of  $p < 0.05$ . The correlation between the quartiles and the FVC, FEV1, and FVC/FEV1 parameters was performed through the Spearman statistical test, establishing a significance of  $p < 0.05$ . The mathematical models to determine the spirometry parameters either in terms of means (S-W with  $p > 0.05$ ) or quartiles (S-W with  $p < 0.05$ ) were obtained from linear regression, establishing a coefficient of determination  $R^2 > 0.5$ . The validation of the obtained data is carried out in case the S-W is greater than 0.05, by means of the T-test for paired data. Otherwise, it is done using the Wilcoxon test. In these tests, a level of significance  $p > 0.05$  was established.

Differences in results were analyzed using a Bland and Altman plot <sup>[17]</sup>.

## RESULTS AND DISCUSSION

### Normality analysis and data representation

The data of the FVC, FEV1 and FEV1/FVC parameters evidenced a normal distribution (S-W  $p > 0.05$ ), therefore, they are represented in terms of means ( $\pm$ SD). The power determinations of the seven frequency segments did not show a normal distribution (S-W  $p < 0.05$ ), so, they are

represented in terms of 25%, 50%, and 75% quartiles. Statistical analysis of these data was performed with Spearman's correlation coefficient and Wilcoxon's test.

The mean values of FVC, FEV1 and FEV1/FVC were  $70\% \pm 14\%$ ,  $46\% \pm 12\%$ , and  $46\% \pm 7\%$ , respectively. The distribution of the powers corresponding to the seven frequency segments obtained from the module and phase are shown in Table 1.

**TABLE 1. Distribution of the powers (in decibels, dB) of the seven frequency segments that make up the changes in pulmonary ventilation obtained by EIT corresponding to the 15 patients with COPD.**

FOI <sup>1</sup> (mHz)	Impedance Module Powers (dB)				Phase Module Powers (dB)			
	Quartile at	Q25% <sup>2</sup>	Q50% <sup>3</sup>	Q75% <sup>4</sup>	Quartile at	Q25% <sup>2</sup>	Q50% <sup>3</sup>	Q75% <sup>4</sup>
0* – 117.49	25%	0.107	0.201	0.279	25%	0.070	0.125	0.306
	50%	0.282	0.309	0.332	50%	0.297	0.333	0.339
	75%	0.373	0.506	0.675	75%	0.388	0.530	0.635
156.66 – 274.15	25%	0.041	0.100	0.135	25%	0.114	0.210	0.248
	50%	0.214	0.292	0.317	50%	0.310	0.330	0.337
	75%	0.479	0.567	0.697	75%	0.433	0.468	0.505
313.32 – 430.18	25%	0.048	0.088	0.164	25%	0.151	0.212	0.290
	50%	0.152	0.211	0.279	50%	0.312	0.330	0.335
	75%	0.523	0.609	0.731	75%	0.376	0.428	0.567
469.98 – 587.47	25%	0.067	0.116	0.207	25%	0.249	0.293	0.314
	50%	0.189	0.271	0.337	50%	0.326	0.333	0.357
	75%	0.509	0.649	0.736	75%	0.350	0.372	0.466
626.64 – 744.13	25%	0.114	0.212	0.258	25%	0.147	0.267	0.314
	50%	0.279	0.312	0.346	50%	0.304	0.333	0.339
	75%	0.396	0.477	0.604	75%	0.359	0.441	0.579
783.30 – 900.79	25%	0.208	0.254	0.289	25%	0.231	0.287	0.306
	50%	0.294	0.331	0.342	50%	0.324	0.333	0.335
	75%	0.371	0.411	0.451	75%	0.352	0.381	0.425
939.95 – 1060	25%	0.239	0.261	0.307	25%	0.220	0.254	0.315
	50%	0.301	0.332	0.340	50%	0.331	0.333	0.343
	75%	0.354	0.391	0.462	75%	0.363	0.414	0.487

<sup>1</sup>FOI: Frequencies of Interest, seven frequency segments in mHz expressed in terms of powers (decibels, dB). The dispersion of these powers is expressed in terms of quartiles (25%, 50%, and 75%) because these data do not show a normal distribution.

<sup>2</sup>Q25%, 25% quartile of power data.

<sup>3</sup>Q50%, 50% quartile of power data.

<sup>4</sup>Q75%, 75% quartile of power data.

\*- zero indicates theoretical value.

### Correlations between spirometry parameters and powers of frequency segments

In the case of the frequency components of the impedance module, significant correlations of approximately 70% were found between: 1) the three quartiles of frequency segment 7 and the FVC; 2) between the 50% quartile of segment 7 and FEV1;

and 3) the 75% quartile of frequency segment 2 and the FEV1/FVC. In the case of the frequency components of the impedance phase, significant correlations of approximately 60% were found between the 25% and 75% quartiles of segments 4 and 7 and the FVC, respectively; and a correlation greater than 70% between the 25% and 75% quartiles of segment 4 and FEV1 (Table 2).

**TABLE 2. Correlations between the powers of the frequency components of the impedance module and phase signals and the spirometric parameters.**

Powers of the frequency components of the module signal and spirometric parameters					Powers of the frequency components of the phase signal and spirometric parameters			
FOI <sup>1</sup>	Quartile at	FVC <sup>2</sup>	FEV1 <sup>3</sup>	FEV1/FVC <sup>4</sup>	FOI <sup>1</sup>	Quartile at	FVC <sup>2</sup>	FEV1 <sup>3</sup>
S7	25%	-0.682	-	-	S4	25%	-0.632	-0.737
	50%	-0.731	-0.732	-		75%	0.646	0.789
S2	75%	0.693	-	-	S7	25%	-0.600	-
	75%	-	-	-0.698		75%	0.661	-

<sup>1</sup>FOI: frequencies of interest: S2 – Segment 2 (156.66 – 274.15 mHz), S4 – Segment 4 (469.98 – 587.47 mHz),

S7 – Segment 7 (939.95 mHz – 1.06 Hz).

<sup>2</sup>FVC: forced vital capacity.

<sup>3</sup>FEV1: forced expiratory volume in the first second.

<sup>4</sup>FEV1/FVC: quotient between the parameters FEV1 and FVC.

### Mathematical fit models

Five equations were obtained that adjust the powers of the impedance signal module to estimate the 3 spirometry parameters. Three determine the estimation of the FVC, one - the FEV1 and the rest - the FEV1/FVC. The mean value of the coefficient of determination (R<sup>2</sup>) of the 5 equations was approximately 54%±11% (Table 3).

Six equations were obtained that adjust the phase powers to estimate two spirometry parameters. Four of these determine the estimation of the FVC and two of the FEV1. The mean value of the R<sup>2</sup> of the 5 equations was approximately 33%±16% (Table 3).

### Evaluation of mathematical fit models

The correlation between measured and estimated determinations for FVC, FEV1, and FEV1/FVC was approximately 76% (p<0.001), 65% (p<0.001), and 69% (p<0.001), respectively (Table 4).

The average value of the dispersion of the measured FVC, FEV1 and FEV1/FVC determinations and those estimated with the impedance modulus equations (Table 3) were 11% (T-Student p=0.903, acceptability at 95%: ±18 %), 19% (T-Student p=0.957, acceptability at 95%: ±19%) and 10% (p=0.655, acceptability at 95%: +11%/-9%), respectively (Figure 1).

**TABLE 3. Linear mathematical models of adjustment for the measurement of the spirometric parameters FVC, FEV1, and FEV1/FVC from the power determinations of the frequency segments.**

Impedance Modulus Equations $y = Ax + B$					Impedance Phase Equations $y = Ax + B$				
Dep.V (y) <sup>1</sup>	Indep.V (x) <sup>2</sup>	Coefficients		R <sup>2</sup>	Dep.V (y) <sup>1</sup>	Indep.V (x) <sup>2</sup>	Coefficients		R <sup>2</sup>
		A	B				A	B	
FVC	S7_25% <sup>3</sup>	-173	115	0.5	FVC	PhS4_25% <sup>7</sup>	-80	92	0.1
	S7_50% <sup>4</sup>	-329	175	0.7		PhS4_75% <sup>8</sup>	100	29	0.3
	S7_75% <sup>5</sup>	148	9	0.6		PhS7_25% <sup>9</sup>	-155	109	0.5
FEV1	S7_50% <sup>4</sup>	-233	120	0.4		PhS7_75% <sup>10</sup>	111	23	0.5
FEV1/FVC	S2_75% <sup>6</sup>	-33	65	0.5		FEV1	PhS4_25% <sup>7</sup>	-90	70
						PhS4_75% <sup>8</sup>	88	11	0.4

<sup>1</sup> Dep.V: Dependent variable of the linear equation.

<sup>2</sup> Indep.V: Independent variable of linear equation.

<sup>3</sup> Quartile at 25% of impedance module power determinations from Segment 7 (939.95 mHz – 1.06 Hz)

<sup>4</sup> Quartile at 50% of impedance module power determinations from Segment 7 (939.95 mHz – 1.06 Hz).

<sup>5</sup> Quartile at 75% of impedance module power determinations from Segment 7 (939.95 mHz – 1.06 Hz).

<sup>6</sup> Quartile at 75% of impedance module power determinations from Segment 2 (156.66 – 274.15 mHz).

<sup>7</sup> Quartile at 25% of impedance phase power determinations from Segment 4 (469.98 – 587.47 mHz).

<sup>8</sup> Quartile at 75% of impedance phase power determinations from Segment 4 (469.98 – 587.47 mHz).

<sup>9</sup> Quartile at 25% of impedance phase power determinations from Segment 7 (939.95 mHz – 1.06 Hz)

<sup>10</sup> Quartile at 75% of impedance phase power determinations from Segment 7 (939.95 mHz – 1.06 Hz).

**TABLE 4. Evaluation of the mathematical linear fit models ( $y = Ax + B$ ) for the estimation of the spirometric parameters FVC, FEV1, and FEV1/FVC.**

Evaluation of the calibration equations of the impedance module					
Parameter	<i>Indep.V (x)</i> <sup>1</sup>	Estimation <sup>2</sup>	Correlation <sup>3</sup>	Error (%) <sup>4</sup>	P-value (T-Student) <sup>5</sup>
FVC	S7_25% <sup>6</sup>	70 ± 10	0.72 (p = 0.002)	12 ± 7	0.937
	S7_50% <sup>7</sup>	70 ± 11	0.81 (p < 0.001)	10 ± 6	0.926
	S7_75% <sup>8</sup>	71 ± 11	0.76 (p = 0.001)	12 ± 6	0.847
FEV1	S7_50% <sup>7</sup>	46 ± 8	0.65 (p = 0.009)	19 ± 14	0.957
FEV1/FVC	S2_75% <sup>9</sup>	45 ± 5	0.69 (p = 0.005)	10 ± 5	0.655
Evaluation of impedance phase calibration equations					
Parameter	<i>Indep.V (x)</i> <sup>1</sup>	Estimation <sup>2</sup>	Correlation <sup>3</sup>	Error (%) <sup>4</sup>	P-value (T-Student) <sup>5</sup>
FVC	PhS4_25% <sup>10</sup>	70 ± 5	0.33 (NS)	15 ± 9	1.000
	PhS4_75% <sup>11</sup>	70 ± 8	0.55 (p = 0.032)	13 ± 7	0.983
	PhS7_25% <sup>12</sup>	70 ± 9	0.68 (p = 0.005)	12 ± 9	0.902
	PhS7_75% <sup>13</sup>	71 ± 10	0.68 (p = 0.005)	12 ± 9	0.824
FEV1	PhS4_25% <sup>10</sup>	45 ± 5	0.42 (NS)	21 ± 16	0.928
	PhS4_75% <sup>11</sup>	47 ± 7	0.65 (p = 0.009)	19 ± 17	0.542

<sup>1</sup> Independent Variable (x) of the adjustment equation. See Table 3.

<sup>2</sup> Estimation of the spirometric parameters from the adjustment equations, see Table 3.

<sup>3</sup> Pearson's correlation between the theoretical spirometric parameters and those estimated with the adjustment equations, see Table 3.

<sup>4</sup> Error percentages of the values estimated with the calibration models of Table 3.

<sup>5</sup> Student's t test statistical p-value.

<sup>6</sup> Quartile at 25% of impedance module power determinations from Segment 7 (939.95 mHz – 1.06 Hz).

<sup>7</sup> Quartile at 50% of impedance module power determinations from Segment 7 (939.95 mHz – 1.06 Hz).

<sup>8</sup> Quartile at 75% of impedance module power determinations from Segment 7 (939.95 mHz – 1.06 Hz).

<sup>9</sup> Quartile at 75% of impedance module power determinations from Segment 2 (156.66 – 274.15 mHz).

<sup>10</sup> Quartile at 25% of impedance phase power determinations from Segment 4 (469.98 – 587.47 mHz).

<sup>11</sup> Quartile at 75% of impedance phase power determinations from Segment 4 (469.98 – 587.47 mHz).

<sup>12</sup> Quartile at 25% of impedance phase power determinations from Segment 7 (939.95 mHz – 1.06 Hz).

<sup>13</sup> Quartile at 75% of impedance phase power determinations from Segment 7 (939.95 mHz – 1.06 Hz).

The correlation between baseline and estimated measurements for FVC and FEV1 was approximately 64% ( $p < 0.05$ ) and 65% ( $p < 0.01$ ), respectively (Table 4). The mean value of the dispersion of the FVC and FEV1 measurements obtained with a spirometer and those estimated using the impedance phase adjustment equations (Table 3) were approximately 13% (mean value of p, 0.927, acceptability at 95%: ±23%) and 20% (mean p-value, 0.735, acceptability at 95%: 20%/-21%) (Figure 2).

The objective of this study was to obtain a set of mathematical calibration models that would allow adjusting the frequency powers of the module and the phase of the impedance changes obtained by EIT to estimate the FVC, FEV1, and FEV1/FVC parameters.

The technique implemented to process the changes in impedance was the analysis of the implicit frequency components of the same ventilatory impedance signal. Unlike a pneumotachometer that only records airflow

variations, the EIT can detect small variations that originate in the lung parenchyma due to air circulation. These are detected by the penetration of the electrical injection current through the thoracic tissue [18] and are evidenced as a carrier or parasitic signals with different amplitudes and frequencies implicit in the signal.

From the analysis of the impedance module and the three spirometry parameters, correlations of approximately 70% were evidenced. The FVC correlated with the three quartiles of segment 7 and 3 adjustment equations were obtained with a mean value of R2 of 60% and with a mean correlation between determinations (measured and estimated) of 76% (error: 11%, p: NS). FEV1 correlated with the quartile at 50% of segment 7, an equation was obtained with an R2 of 40% with a correlation between measurements of 65% (error: 20%, p: NS). And the FEV1/FVC ratio with the quartile at 75% of segment 2, an equation with an R2 of 50% and a correlation of 60% was obtained (error: 10%, p: NS).

### Bland and Altman plots to estimate FVC from the modulus powers of the impedance signal

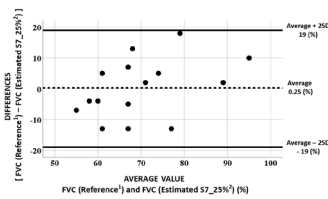


Fig. 1.1 Estimated FVC S7\_25%

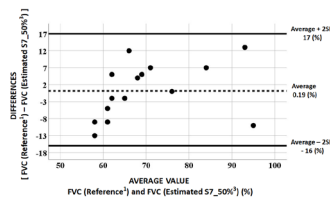


Fig. 1.2 Estimated FVC S7\_50%

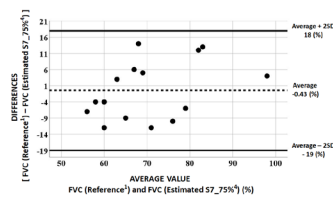


Fig. 1.3 Estimated FVC S7\_75%

### Bland and Altman plots to estimate FEV1 from the modulus powers of the impedance signal

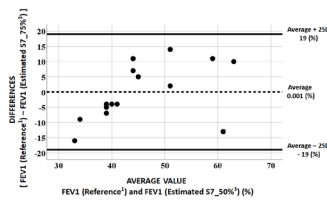


Fig. 1.4 Estimated FEV1 S7\_50%

### Bland and Altman plots to estimate FEV1/FVC from the modulus powers of the impedance signal

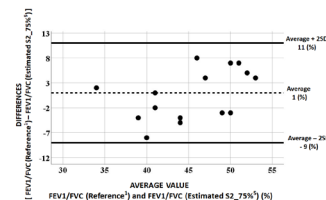


Fig. 1.5 Estimated FEV1/FVC S2\_75%

<sup>1</sup>FVC, FEV1, and FEV1/FVC parameters measured with a spirometer.

<sup>2</sup>Adjustment equation to estimate FVC determined by the quartile at 25% of the data corresponding to segment 7 (Table 3).

<sup>3</sup>Adjustment equation to estimate FVC determined by the quartile at 50% of the data corresponding to segment 7 (Table 3).

<sup>4</sup>Adjustment equation to estimate FVC determined by the quartile at 75% of the data corresponding to segment 7 (Table 3).

<sup>5</sup>Adjustment equation to estimate FEV1/FVC determined by the quartile at 75% of the data corresponding to segment 2 (Table 3).

**FIGURE 1. Analysis of differences in spirometric parameters (FVC, FEV1, and FEV1/FVC) obtained using spirometry equipment and those obtained based on the powers of the impedance change module obtained using an electrical impedance tomography system.**

From the analysis of the frequency spectrum of the phase and the spirometry parameters, the FVC and FEV1 showed significant correlations of approximately 60%. The FVC with the Q25% and Q75% quartile of segments 4 and 7, respectively. Four equations were obtained with a mean R2 of 35% and a correlation between determinations of 64% (error: 13%, p: NS). Finally, the FEV1 with the quartiles at 25% and 75% of segment 4, two mathematical models were obtained with a mean R2 of 30%, and a correlation between determinations of 54% (error: 20%, p: NS).

Other research groups have proposed various techniques to process EIT changes. The parameters derived from the processing have been correlated with the spirometry parameters. Milne *et al.* [19] propose to characterize ventilatory heterogeneity (HV) from a series

of estimated parameters of the changes in circulating volume obtained by means of EIT. Five determinations were obtained from each element of the EIT images: 1) half-expiratory time (tE), 2) the average difference between the temporal impedance changes of each pixel and the impedance variations corresponding to the entire image (Phase), 3) the mean amplitude of the impedance changes ( $\Delta Z$ ), 4) the coefficient of variation (CV) and 5) the index of heterogeneity (IH). The CV was defined as the ratio of the standard deviation and the average of the impedance changes obtained in the entire EIT image.

The IH was estimated in a region of interest (ROI) of 25 pixels where the pixel of interest was located in the center of the ROI. The regional CV value is assigned to the pixel of interest. This value was defined as the



## Bland and Altman plots to estimate FVC from impedance signal phase powers

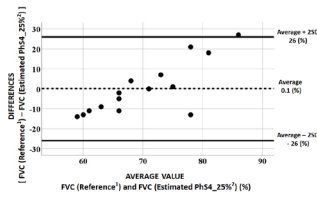


Fig. 2.1 FVC estimated PhS4\_25%

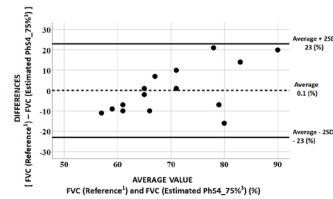


Fig. 2.2 FVC estimated PhS4\_75%

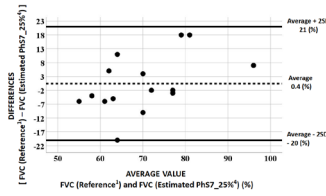


Fig. 2.3 FVC estimated PhS7\_25%

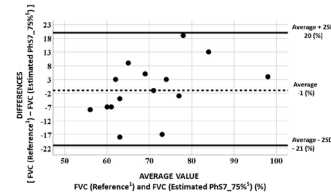


Fig. 2.4 FVC estimated PhS7\_75%

## Bland and Altman plots to estimate FEV1 from impedance signal phase powers

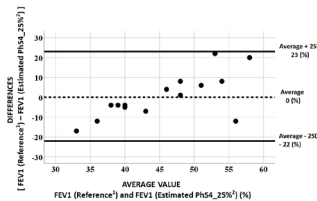


Fig. 2.5 FEV1 estimated PhS4\_25%

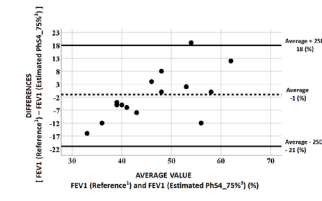


Fig. 2.6 FEV1 estimated PhS4\_75%

<sup>1</sup> FVC, FEV1, and FEV1/FVC parameters measured by a spirometer.

<sup>2</sup> Adjustment equation to estimate FVC determined by the quartile at 25% of the phase powers of segment 4 (Table 3).

<sup>3</sup> Adjustment equation to estimate FVC determined by the quartile at 75% of the powers of the phase of segment 4 (Table 3).

<sup>4</sup> Adjustment equation to estimate FVC determined by the quartile at 25% of the powers of the phase of segment 7 (Table 3).

<sup>5</sup> Adjustment equation to estimate FVC determined by the quartile at 75% of the powers of the phase of segment 7 (Table 3).

**FIGURE 2. Analysis of differences in spirometric parameters (FVC, FEV1, and FEV1/FVC) obtained using spirometry equipment and obtained based on the phase powers of impedance changes obtained using an electrical impedance tomography system.**

Local Heterogeneity Score (LHS). The ROI then moves to its adjacent position and starts the regional CV estimation and LHS assignment again. The estimation cycle ends when the LHS is assigned to each pixel of the image. From the results obtained based on the Phase of the EIT impedance signal, a correlation between FEV1 and the CV and IH parameters of  $r = -0.59$  ( $p = 0.01$ ) and  $r = -0.53$  ( $p = 0.02$ ) was evidenced, respectively. And a correlation between FEV1/FVC and CV and IH parameters of  $r = -0.4$  ( $p = 0.03$ ) and  $r = -0.38$  ( $p = 0.1$ ), respectively [19]. Lasarow *et al.* [20] propose the

use of EIT for monitoring forced pulmonary ventilation using regions of interest and for estimating the parameters used in [19], CV and IH. Correlations between FVC and CV and IH parameters of  $r = -0.1515$  ( $p = 0.0903$ ) and  $r = -0.1534$  ( $p = 0.0864$ ), respectively, were evidenced. From the analysis of FEV1 and the CV and IH parameters, a correlation of  $r = -0.2758$  ( $p = 0.0018$ ) and  $r = -0.2799$  ( $p = 0.0015$ ) was evidenced, respectively [20].

The comparison of the results obtained in [19], [20] and those obtained in this study are shown in Table 5.

TABLE 5. Comparison of results obtained between research groups.

Parameters	Milne <i>et al.</i> (2019) [19] <sup>1</sup>		Lasarow <i>et al.</i> (2021) [20] <sup>2</sup>		Present study	
	CV <sup>3</sup>	HI <sup>4</sup>	CV <sup>3</sup>	HI <sup>4</sup>	TRF-Module <sup>5</sup>	TRF-Phase <sup>6</sup>
FVC			-0.15 (p=0.0903)	-0.15 (p=0.0864)	0.76 (p<0.05)	0.64 (p<0.05)
FEV1	-0.59 (p=0.01)	-0.53 (p=0.02)	-0.28 (p=0.0018)	-0.28 (p=0.0015)	0.65 (p<0.05)	0.54 (p<0.05)
FEV1/FVC	-0.40 (p=0.03)	-0.38 (p=0.1)			0.60 (p<0.05)	

The results obtained in this study were significantly superior to those found by Milne *et al.* [19] by 6% and 34% for FEV1 and FEV1/FVC, respectively. And those found by Lasarow *et al.* [20] in 79% and 53% for the FVC and FEV1 parameters, respectively.

The next step of the investigation will be to find a relationship between the spirometry parameters and the impedance changes using an array of four electrodes. This study will demonstrate the feasibility of using simpler and less expensive impedance equipment to be used in the clinical field on an outpatient basis.

### CONCLUSIONS

EIT impedance changes due to pulmonary ventilation are composed of signals of different amplitudes and frequencies that are the result not only of chest movements but also of the behavior of the lung parenchyma conditioned by the flow of circulating air. These frequencies correlate with the spirometry parameters FVC, FEV1, and FEV1/FVC. FVC and FEV1 show a statistically significant correlation in the frequency range between 939.95mHz and 1.06Hz and FEV1/FVC in the range between 156.66mHz - 274.15mHz. The calibration equations conditioned by each frequency component and intended for the estimation of the spirometry parameters showed a sufficient mathematical adjustment to obtain estimates comparable to those of the reference values. This monitoring technique could be used in patients to determine the degree of pulmonary obstruction/restriction non-invasively and only with monitoring of circulating volume.

### AUTHOR CONTRIBUTIONS

F. M. V. L. conceptualized the project, curated data, developed the methodology, carried out formal analyses, performed bibliographical research and investigated in order to carry out the project, and participated in the writing of the original manuscript. S. K. conceptualized the project, curated data and validated, carried out formal analyses, developed the methodology, participated in the writing, reviewing and editing the manuscript. P. J. R. C. performed bibliographical research and investigation for the project and validated data, developed the methodology, performed bibliographical research and investigation, and participated in the writing, reviewing and editing the manuscript. P. C. C. performed bibliographical research and investigation for the project, developed the methodology, performed bibliographical research and investigation and validated data, participated in the writing, reviewing and editing the manuscript. J. M. B. O. conceptualized the project, curated data, developed the methodology, performed bibliographical research and investigation for the project, provided funding, oversaw the general progress of the project and provided resources, contributed to writing the draft and final version of the manuscript, reviewed and edited comments. All authors reviewed and approved the final version of the manuscript.

### Ethical statement

This study was approved by the Ethical Committee of the University of Guanajuato with code CIBIUG-A56-2019.

## REFERENCES



- [1] Instituto Nacional de Estadística, Geografía e Informática (INEGI). Mortality dataset, distributed by INEGI. [Internet]. 2022. Available from: <https://www.inegi.org.mx/programas/mortalidad/#Tabulados>
- [2] Global Initiative for Chronic Obstructive Lung Disease. 2022 Gold Reports [Internet]. 2022. Available from: [https://goldcopd.org/wp-content/uploads/2021/12/GOLD-REPORT-2022-v1.1-22Nov2021\\_WMV.pdf](https://goldcopd.org/wp-content/uploads/2021/12/GOLD-REPORT-2022-v1.1-22Nov2021_WMV.pdf)
- [3] Halpin DMG, Criner GJ, Papi A, Singh D, et al. Global Initiative for the Diagnosis, Management, and Prevention of Chronic Obstructive Lung Disease. The 2020 GOLD Science Committee Report on COVID-19 and Chronic Obstructive Pulmonary Disease. *Am J Respir Crit Care Med* [Internet]. 2021;203(1):24-36. Available from: <https://doi.org/10.1164/rccm.202009-3533SO>
- [4] Virani A, Baltaji S, Young M, Dumont T, et al. Chronic Obstructive Pulmonary Disease: Diagnosis and GOLD Classification. *Crit Care Nurs Q* [Internet]. 2021;44(1):9-18. Available from: <https://doi.org/10.1097/CNQ.0000000000000335>
- [5] Hernández-Ruiz A, Ortega HJ, Aguirre-Acevedo DC. Utilidad de la espirometría en los pacientes hospitalizados por la enfermedad pulmonar obstructiva crónica (EPOC) exacerbada. *Iatreia* [Internet]. 2020;33(4):341-347. Available from: <https://revistas.udea.edu.co/index.php/iatreia/article/view/339541>
- [6] Zhao Z, Fu F, Frerichs I. Thoracic electrical impedance tomography in Chinese hospitals: a review of clinical research and daily applications. *Physiol Meas* [Internet]. 2020;41(4):04TR01. Available from: <https://doi.org/10.1088/1361-6579/ab81df>
- [7] Karagiannidis C, Waldmann AD, Róka PL, Schreiber T, et al. Regional expiratory time constants in severe respiratory failure estimated by electrical impedance tomography: a feasibility study. *Crit Care* [Internet]. 2018;22(1):221. Available from: <https://doi.org/10.1186/s13054-018-2137-3>
- [8] Vogt B, Zhao Z, Zabel P, Weiler N, et al. Regional lung response to bronchodilator reversibility testing determined by electrical impedance tomography in chronic obstructive pulmonary disease. *Am J Physiol Lung Cell Mol Physiol* [Internet]. 2016;311(1):L8-L19. Available from: <https://doi.org/10.1152/ajplung.00463.2015>
- [9] Tang Y, Turner MJ, Yem JS, Baker AB. Calibration of pneumotachographs using a calibrated syringe. *J Appl Physiol* [Internet]. 2003;95(2):571-576. Available from: <https://doi.org/10.1152/jappphysiol.00196.2003>
- [10] de Lema B, Casan P, Riu PJ. Electrical Impedance Tomography: Standardizing the Procedure in Pneumology. *Arch Bronconeumol* [Internet]. 2006;42(6):299-301. Available from: [https://doi.org/10.1016/s1579-2129\(06\)60146-8](https://doi.org/10.1016/s1579-2129(06)60146-8)
- [11] Balleza Ordaz JM. Monitorización del patrón ventilatorio (PV) mediante tomografía por impedancia eléctrica (TIE) en paciente con enfermedad pulmonar obstructiva crónica (EPOC) [Ph.D.'s thesis]. [Cataluña]: Universitat Politècnica de Catalunya, 2012. 261p. Spanish. Available from: <https://upcommons.upc.edu/bitstream/handle/2117/94737/TJBO1de1.pdf;jsessionid=A8A27A61BBD1417D29C2D0179ED3DAAC?sequence=1>
- [12] Serrano RE, de Lema B, Casas O, Feixas T, et al. Use of electrical impedance tomography (TIE) for the assessment of unilateral pulmonary function. *Physiol Meas* [Internet]. 2002;23(1):211. Available from: <https://doi.org/10.1088/0967-3334/23/1/322>
- [13] Casas O, Rosell J, Bragós R, Lozano A, et al. A parallel broadband real-time system for electrical impedance tomography. *Physiol Meas* [Internet]. 1996;17(4A):A1. Available from: <https://doi.org/10.1088/0967-3334/17/4A/002>
- [14] Python, version 3.10 [Internet]. Python Software Foundation; 2022. Available from: <https://www.python.org/downloads/release/python-3104/>
- [15] Smith SW. *The Scientist and Engineer's Guide to Digital Signal Processing* [Internet]. San Diego: California Technical Publishing; 1999. Available from: <https://www.dspguide.com/>
- [16] Weeks M. *Digital Signal Processing: using MATLAB and wavelets*. Massachusetts: Jones & Bartlett Learning; 2007. 492p.
- [17] Braždžionytė J, Macas A. Bland-Altman analysis as an alternative approach for statistical evaluation of agreement between two methods for measuring hemodynamics during acute myocardial infarction. *Medicina* [Internet]. 2007;43(3):208. Available from: <https://doi.org/10.3390/medicina43030025>
- [18] Grimnes S, Martinsen OG. *Bioimpedance and bioelectricity basics* [Internet]. Oxford: Academic Press; 2008. 488p. Available from: <https://www.sciencedirect.com/book/9780123740045/bioimpedance-and-bioelectricity-basics>
- [19] Milne S, Huvanandana J, Nguyen C, Duncan JM, et al. Time-based pulmonary features from electrical impedance tomography demonstrate ventilation heterogeneity in chronic obstructive pulmonary disease. *J Appl Physiol* [Internet]. 2019;127(5):1441-1452. Available from: <https://doi.org/10.1152/jappphysiol.00304.2019>
- [20] Lasarow L, Vogt B, Zhao Z, Balke L, et al. Regional lung function measures determined by electrical impedance tomography during repetitive ventilation maneuvers in patients with COPD. *Physiol Meas* [Internet]. 2021;42:015008. Available from: <https://iopscience.iop.org/article/10.1088/1361-6579/abdad6>

[dx.doi.org/10.17488/RMIB.43.3.4](https://dx.doi.org/10.17488/RMIB.43.3.4)

E-LOCATION ID: 1317

## Reseña del Libro: “Medicine-Based Informatics and Engineering” Lecture Notes in Bioengineering, Springer, 2022

### Book Review: “Medicine-Based Informatics and Engineering” Lecture Notes in Bioengineering, Springer, 2022

Néstor Darío Duque-Méndez  

Universidad Nacional de Colombia - Colombia

#### RESUMEN

El presente trabajo es una reseña original sobre el libro “*Medicine-Based Informatics and Engineering*” publicado en la colección *Lecture Notes in Bioengineering de Springer*, en 2022, cuyos editores son los investigadores Franco Simini y Pedro Bertemes-Filho. La reseña busca sintetizar el contenido de los trabajos presentados en los capítulos centrándose en las soluciones desarrolladas. Los editores, a partir de la diversidad de los aportes, vislumbran la integración de visiones, en lo que denominan “Ingeniería Médica”.

**PALABRAS CLAVE:** Ingeniería biomédica, informática médica, ingeniería médica

### ABSTRACT

This paper is an original review of the book "Medicine-Based Informatics and Engineering" published in Springer's Lecture Notes in Bioengineering collection, in 2022, whose editors are Franco Simini and Pedro Bertemes-Filho. The review aims to synthesize the content of the papers presented in the chapters focusing on the solutions developed. The editors, from the diversity of the contributions, envision the integration of visions, in what they call "Medical Engineering".

**KEYWORDS:** Biomedical engineering, medical informatics, medical engineering

#### Corresponding author

TO: Néstor Darío Duque-Méndez

INSTITUTION: Departamento de Informática y  
Computación Campus La Nubia Bloque Q

Universidad Nacional de Colombia

ADDRESS: CL. 65#23-29, Manizales Caldas, Colombia

CORREO ELECTRÓNICO: [ndduqueme@unal.edu.co](mailto:ndduqueme@unal.edu.co)

#### Received:

11 October 2022

#### Accepted:

16 November 2022

## RESEÑA

Los editores del libro reseñado son los investigadores Franco Simini y Pedro Bertemes-Filho y el libro fue publicado en la colección *Lecture Notes in Bioengineering de Springer*, en 2022<sup>[1]</sup>.

El libro recoge trabajos de investigadores de siete países donde exponen el desarrollo de diferentes artefactos de hardware y software orientados a mejorar la atención médica desde diferentes enfoques interdisciplinarios integrando capacidades en áreas de salud, ingeniería y tecnologías de alto impacto. Términos como Ingeniería Biomédica (BME) e Informática Médica (MI) se concretan y fusionan en soluciones específicas, producto de los retos, necesidades y posibilidades en la vida diaria y como centro buscan beneficiar la práctica profesional pero fundamentalmente la calidad de vida y el bienestar de la sociedad.

Es claro que la Cuarta Revolución Industrial 4RI, sus tecnologías e impacto social están presentes en estas páginas. Las tecnologías emergentes relacionadas con la 4RI son fundamentalmente inteligencia artificial, análisis de datos, manufactura aditiva, realidad virtual y/o aumentada, robótica e Internet de las cosas (IoT). En los trabajos expuestos en el libro se aprovechan conceptos relacionados y se ofrecen aplicaciones en diferentes escenarios, que involucran técnicas relacionadas con la 4RI.

A continuación, se hará un breve recorrido por los capítulos que conforman el libro.

En el primer capítulo el profesor Franco Simini, hace presentación de proyectos seleccionados de BME e MI que tienen como resultado artefactos de hardware y software y que fueron desarrollados por equipos interdisciplinarios en el Núcleo de Ingeniería Biomédica de la Universidad de la República en Uruguay. Software orientado a seguimiento Perinatal Personalizado, App

(aplicación móvil) de recetas personalizadas, pero también hardware como dispositivos de medición de torque/velocidad, campana de vacío servocontrolada para tratar hipertensión intraabdominal y un artefacto para una medida no invasiva de volumen renal poliúístico se abren pasos en esta sección del libro.

Por interés personal me ha llamado la atención el sistema *PRAXIS*, que reconoce los mecanismos de razonamiento humano que aprovecha la experiencia previa para enfrentar nuevos problemas y el sistema utiliza el caso actual para generar evidencia consolidada de "tipos de casos" existentes o nuevos, que apoyan la toma de decisiones. Esta aplicación retoma, desde la *PRAXIS*, lo que en inteligencia artificial se conoce como Razonamiento Basado en Casos (CBR), una técnica muy prometedora en aplicaciones diversas... valdría la pena formalizar el modelo. El autor devela una crítica a los sistemas de registros clínicos basados en una traducción ingenua de sistemas de información sin diseño interdisciplinario, que restan valor a la solución ante la ausencia de la sinergia medicina-tecnología.

En el capítulo 2 los autores, investigadores del Politécnico di Torino encabezados por Valentina Agostini, resaltan la importancia del análisis de la marcha con información de la actividad eléctrica de los músculos durante la tarea dinámica de caminar, capturada a través de sondas de electromiografía de superficie (sEMG). A la vez reconocen que las señales sEMG deben procesarse a través de técnicas avanzadas para obtener resultados confiables, fácilmente interpretables por los profesionales de la salud. Orientado a este objetivo, aplican técnicas basadas en algoritmos de procesamiento de última generación de la señal sEMG y presentan un análisis automático estadístico de la marcha (SGA) de cientos de ciclos recopilados durante una caminata fisiológica o patológica de varios minutos. Extraen las activaciones musculares principales y secundarias para obtener índices clínicos y proceder a la extracción de sinergias musculares para estudiar

cuantitativamente las estrategias de control motor.

El capítulo 3 fue escrito por los investigadores de Argentina, L. Carolina Carrere, Carlos H. Ballarío y Carolina B. Tabernig de la Universidad Nacional de Entre Ríos, Fundación Rosarina de Neurorehabilitación y el Instituto NeuroRosario, respectivamente. En la sección se describe la estructura general y el funcionamiento de interfaces cerebro-computadora (BCI) - una tecnología emergente que está generando grandes impactos- que utilizan *Functional Electrical Stimulators* (FES) de superficie como dispositivo actuador, utilizados para recuperar el agarre y liberación de objetos y/o la dorsiflexión del pie durante la marcha, entre otros. Los autores muestran dos aplicaciones terapéuticas de BCI-FES para la neurorehabilitación motora de pacientes con accidente cerebrovascular y esclerosis múltiple, con muy buenos resultados funcionales motores. Estas dos aplicaciones son ejemplos de colaboración interdisciplinaria entre médicos e investigadores de ingeniería biomédica para presentar una solución tecnológica emergente para mejorar la calidad de vida de los pacientes.

En el capítulo 4 se presentan los retos y riesgos de los sistemas de adquisición de biopotenciales en ambientes menos controlados y orientados a monitoreo las 24 horas a través de conexiones de datos digitales en red. El diseño amplificadores biopotenciales en estas condiciones requiere dispositivos portátiles confiables, de bajo costo y facilidad de uso. Se discute una situación a resolver: la compensación entre el rango dinámico, el rango de frecuencia y el consumo de energía que debe definirse considerando las características específicas de la señal biopotencial. Para los autores, en las aplicaciones concretas se deben enfrentar asuntos que afectan el rendimiento de la interfaz analógica, las topologías de medición, puesta a tierra y estrategias de administración de voltaje, el análisis de interferencia de la línea eléctrica y un análisis de artefactos de movimiento y filtrado. Una amplia gama de componentes

comerciales soporta la construcción y puesta en funcionamiento de estos sistemas, tanto a nivel de manejo de señales y procesamiento como de elementos de comunicación que se benefician de infraestructuras ubicuas como Bluetooth, Wifi o redes móviles para la transmisión de datos. Los autores del capítulo son Federico N. Guerrero y Enrique M. Spinelli del Instituto de Investigaciones en Electrónica, Control y Procesamiento de Señales LEICI de la Universidad Nacional de Plata, Argentina.

Investigadores de la Universidade do Estado de Santa Catarina, Joinville en Brasil, son los autores del capítulo 5 dedicado a exponer dispositivos vestibles (*Wearable*) de medición de bioimpedancia. Bertemes-Filho y Morcelles, los autores, resaltan la importancia de la técnica *Electrical Bioimpedance* (BIA) una tecnología innovadora que contribuye a reducir costos y tiempo en la caracterización de materiales biológicos, mostrando usos en detección de tejidos cancerosos, composición corporal, glucómetro en sangre, medidor de calidad de agua y leche bovina. Pero esta función de diagnóstico basada en mediciones de impedancia requiere un modelo matemático para reducir los posibles valores de incertidumbre y es deseable hardware de bajo consumo de energía y de conexiones inalámbrica. A partir de estas reflexiones en esta sección se presenta lo que los autores denominan "*Wearable Bioimpedance Measuring Devices*" con conceptos, diseño de circuitos y propuesta para el análisis de datos.

Ricardo Armentano de la Universidad de la República, en el capítulo 6, diserta sobre ingeniería cardiovascular predictiva mostrando los espacios abiertos para transformar los datos en conocimientos futuros sobre enfermedades cardiovasculares. Estas enfermedades son la principal causa de muerte para ambos sexos en el mundo occidental. La exploración no invasiva de los vasos humanos basada en avances tecnológicos permite detectar alteraciones preclínicas en pacientes asintomáticos, lo que contribuye a la medicina preven-

tiva, que tomará una relevancia cada vez mayor en los próximos años. El autor concluye que “modelos físico-matemáticos que integren todos los factores hemodinámicos cardiovasculares podrían ser de gran interés en la práctica clínica diaria para predecir la ocurrencia de eventos cardíacos con mayor detalle que con el uso de factores de riesgo tradicionales”. Se manifiesta en el capítulo que el enfoque cardiometabólico se centró en la ingeniería del sistema arterial, aplicando Física a las ciencias de la vida en un entorno realista en el dominio de la Fisiología Integrativa. Un elemento que se resalta es que los organismos vivos son sistemas dinámicos altamente complejos, pues son multi-alimentados, no lineales y con cierta organización jerárquica. Esta complejidad exige que el componente teórico se integre en un todo con el trabajo experimental. Como lo dice el autor, son varias las alternativas que permiten este enfoque y juegan un papel importante en la investigación, desarrollo y gestión de tecnologías médicas: dispositivos médicos portátiles; hemodinámica y biomecánica tisular; ingeniería de tejidos y medicina regenerativa; aprendizaje automático, análisis predictivo e IoT; y “que tienden a cumplir con el término Bench to Bedside utilizado para describir el proceso por el cual los resultados de la investigación realizada en el laboratorio se utilizan directamente para desarrollar nuevas formas de tratar a los pacientes”.

Investigadoras del Departamento de Ingeniería eléctrica de la Universidad Autónoma Metropolitana-Iztapalapa en México son las autoras del capítulo 7 orientado a Ingeniería de Dispositivos Médicos Especiales para grupos vulnerables mediante la descripción de la experiencia en dos hospitales estatales de México con poblaciones vulnerables. El primer caso está relacionado con el grupo vulnerable de mujeres pobres con embarazos de alto riesgo, atendido mediante el diseño y construcción de un prototipo de sistema de perfusión para cotiledón de placenta humana que permite estudiar fármacos para el cuidado intensivo de la paciente obstétrica y posible afectación al feto en el

útero. El segundo caso se asocia con niños en situación de pobreza, que presentan labio leporino y/o paladar hendido y el proyecto se orienta al desarrollo de una herramienta computacional que ayude al médico cirujano en la evaluación y pronóstico de la rehabilitación de pacientes que presentan estas malformaciones congénitas. Los autores concluyen que los resultados son alentadores y se abre un camino para futuros trabajos.

El capítulo 8, a cargo de investigadores de la Universidad Feevale en el sur de Brasil, es titulado “Juegos Serios y Realidad Virtual para Rehabilitación y Seguimiento de Personas en Silla de Ruedas”, aprovecha las tecnologías emergentes asociadas a la 4RI. Se describe la implantación de un ambiente de realidad virtual, usando gafas Gear-VR, para uso en fisioterapia con pacientes en silla de ruedas y busca mejorar el control del tronco. El sistema consiste en una serie de minijuegos que incorporan nuevos movimientos y actividades. Es un esfuerzo interdisciplinario, como la mayor parte de las propuestas del Libro, que destaca roles a cada profesional involucrado: el fisioterapeuta debe configurar los ángulos de movimiento según las necesidades del paciente para que los expertos en informática y juegos creen el ambiente que promueva los movimientos establecidos, a la vez que se pueda seguir la evolución del paciente tanto en la sesión cuanto en el tratamiento. Es un enfoque interesante y llamativo pendiente de validar en la clínica.

Investigadores Bulc, Hart, Hannah y Hrovatin, de Slovenia y del Reino Unido, nos introducen, en el siguiente capítulo, en el mundo de la Sociedad 5.0 que nos debe llevar hacia una sociedad centrada en el ser humano; donde se equilibren los desarrollos económicos, políticos, sociales y personales desde lo colectivo, y donde las interdependencias ofrezcan soluciones colectivas. Acorde a esto, los autores manifiestan que la Sociedad 5.0 requiere un ecosistema de salud centrado en el ser humano (Salud 5.0) que se caracterice por un alto nivel de transparencia e integración de soluciones



digitales y de inteligencia artificial como herramientas de apoyo. La Sociedad 5.0 está enmarcada en la 4RI que conlleva la adopción masiva de las tecnologías, como internet de las cosas (IOT), la inteligencia artificial, entre otras, que replantean las dinámicas sociales esperanzadoras, pero también intimidadoras. En estas páginas se deja ver que las TIC y la inteligencia artificial son imprescindibles en el mundo de la medicina, pero los autores afirman que estas tecnologías deben estar al servicio de los profesionales de la salud y no deben ser las que rigen las acciones en salud. Los autores exponen el componente político relacionado con la Salud 5.0, para luego mostrar, desde el pensamiento sistémico en medicina, los enfoques de atención centrados en la persona o, para los autores, el nuevo paradigma de la medicina personalizada o de precisión. Continúan con el marco cognitivo para las prácticas de atención médica dejando claro que esto impone límites al valor de las soluciones tecnológicas para lograr resultados positivos en salud. Para reforzar su propuesta exponen un ejemplo de la vida real.

En el capítulo 10, el autor Díaz Berenguer de la Universidad de la Republica en Uruguay enfrenta un tema de actualidad: la relación Médico-Paciente e Informática en la práctica clínica. En este trabajo se le considera como un tipo especial de comunicación, la relación médico-paciente que aprovecha simultáneamente múltiples lenguajes y códigos, todos ellos propios de la interacción humana. Se parte de la intencionalidad del que espera ser sanado y del que espera poder sanar y esta comunicación se beneficia de los gestos, el lenguaje corporal, las miradas y otras sensaciones además del escenario y vestuario usado. El autor manifiesta la preocupación de que se pueda alterar este rico y complejo canal de comunicación ante la introducción de los computadores, al menos como se utilizan en la actualidad puedan convertirse en un obstáculo para una adecuada relación médico-paciente y oculte a uno del otro, con los efectos que esto podría traer. ¿Será que acá hay espacio para la computación-

fectiva, un enfoque que gana espacio en diferentes ambientes?

Se cierra este interesante libro con el capítulo Colaboración interdisciplinaria dentro de la informática basada en la medicina e ingeniería para el impacto social, de los investigadores Simini de Uruguay y Vienni de Suiza; quienes presentan las oportunidades y desafíos, en el ámbito nacional e internacional, que se enfrentan los procesos de colaboración interdisciplinarios, en particular desde la Medicina, la Informática y la Ingeniería, que es el mecanismo por excelencia para atacar los desafíos sociales actuales con impacto real. Se analiza una experiencia exitosa, que data de 40 años atrás: el Núcleo de Ingeniería Biomédica en la Universidad de la República en Uruguay, presentando las lecciones aprendidas narrativas exitosas tanto en líneas de investigación generales como específicas. Este capítulo, como los demás del Libro dejan en claro la importancia de BME y MI en la solución de problemas de salud y bienestar social aprovechando diferentes tecnologías de hardware y software, pero sobre todo entendiendo que se debe involucrar a los diferentes actores para lograr los resultados esperados.

Para cerrar es necesario decir que este libro, además de exponer los trabajos de los autores, invita a la reflexión sobre las posibilidades abiertas para enfrentar problemáticas desde diferentes ópticas y con artefactos provenientes de campos disímiles que se conjugan para obtener soluciones, de las cuales hasta ahora se ve la punta del iceberg.

El lector experimentado se encontrará con llamativos e ingeniosos desarrollos que pueden extenderse y aplicarse a otro tipo de situaciones con mente creativa e innovadora. Pero al lector que apenas se introduce en las profundas aguas de las tecnologías en medicina, le abre un espectro inmenso tanto desde la exploración de las tecnologías emergentes, como de su aplicación

armónica con el bagaje en investigación en salud para acercarse a soluciones tangibles, aplicables en la cotidianidad clínica.

Como nota final quiero resaltar que los editores dejan abierta una discusión al plantear que, a partir de los avances en la integración, podría hablarse de "Ingeniería Médica" para incluir a las actuales Ingeniería Biomédica o *Biomedical Engineering* (BME) y la Informática Médica o *Medical Informatics* (MI).

## REFERENCIAS








- [1] Simini F, Bertemes-Filho P (eds.). Medicine-Based Informatics and Engineering [Internet]. Cham, Switzerland: Springer; 2022. Pp. 201. Available from: <https://doi.org/10.1007/978-3-030-87845-0>

[dx.doi.org/10.17488/RMIB.43.3.5](https://dx.doi.org/10.17488/RMIB.43.3.5)

E-LOCATION ID: 1304

## Detection of People Positive to COVID-19 through ATR-FTIR Spectra Analysis of Saliva using Machine Learning

### Detección de Personas Positivas a COVID-19 mediante el Análisis de Espectros ATR-FTIR de Muestras de Saliva empleando Machine Learning

Gustavo Jesús Vazquez-Zapien<sup>1</sup> , Monica Maribel Mata-Miranda<sup>1</sup> , Adriana Martinez-Cuazitl<sup>1</sup> ,  
Melissa Guerrero-Ruiz<sup>1</sup> , Francisco Garibay-Gonzalez<sup>1</sup> , Miguel Sanchez-Brito<sup>2</sup>  

<sup>1</sup>Escuela Militar de Medicina, Centro Militar de Ciencias de la Salud, Secretaría de la Defensa Nacional, Ciudad de México - México

<sup>2</sup>Instituto Politécnico Nacional, Escuela Superior de Cómputo, Ciudad de México - México

#### ABSTRACT

COVID-19 is an infectious disease caused by the SARS-CoV-2 virus. This virus's spread is mainly through droplets released from the nose or mouth of an infected person. Although vaccines have been developed that effectively reduce the effects that this viral infection causes, the most effective method to contain the virus's spread is numerous tests to detect and isolate possible carriers. However, the response time, combined with the cost of actual tests, makes this option impractical. Herein, we compare some machine learning methodologies to propose a reliable strategy to detect people positive to COVID-19, analyzing saliva spectra obtained by Fourier transform infrared (FTIR) spectroscopy. After analyzing 1275 spectra, with 7 strategies commonly used in machine learning, we concluded that a multivariate linear regression model (MLMR) turns out to be the best option to identify possible infected persons. According to our results, the displacement observed in the region of the amide I of the spectrum, is fundamental and reliable to establish a border from the change in slope that causes this displacement that allows us to characterize the carriers of the virus. Being more agile and cheaper than reverse transcriptase polymerase chain reaction (RT-PCR), it could be reliably applied as a preliminary strategy to RT-PCR.

**KEYWORDS:** Saliva, ATR-FTIR, machine learning, COVID-19, diagnosis.

## RESUMEN

La COVID-19 es una enfermedad infecciosa ocasionada por el virus SARS-CoV-2. La propagación de este virus se produce principalmente a través de gotitas liberadas por la nariz o la boca de una persona infectada. Aunque se han desarrollado vacunas que permiten reducir efectivamente los efectos que esta infección viral provoca, el método más eficaz para contener la propagación del virus son las numerosas pruebas para detectar y aislar los posibles portadores. Sin embargo, el tiempo de respuesta, combinado con el costo de las pruebas reales, hace que esta opción sea poco práctica. Aquí, comparamos algunas metodologías de machine learning para proponer una estrategia confiable para detectar personas positivas a COVID-19 analizando espectros de saliva obtenidos por espectroscopia infrarroja transformada de Fourier (FTIR). Tras analizar 1275 espectros, con 7 estrategias comúnmente empleadas en el área de machine learning, concluimos que un modelo de regresión lineal multivariante (MLMR) resulta ser la mejor opción para identificar posibles infectados. De acuerdo con nuestros resultados, el desplazamiento observado en la región de la amida I del espectro, resulta fundamental y confiable para establecer una frontera a partir del cambio de pendiente que este provoca. Al ser más ágil y económica que la reacción en cadena de la polimerasa con transcriptasa inversa (RT-PCR), podría aplicarse confiablemente como estrategia preliminar a RT-PCR.

**PALABRAS CLAVE:** Saliva, ATR-FTIR, aprendizaje máquina, COVID-19, diagnóstico.

### Corresponding author

TO: Miguel Sánchez-Brito

INSTITUTION: Instituto Politécnico Nacional, Escuela Superior de Cómputo

ADDRESS: Av. Luis Enrique Erro S/N, Nueva Industrial Vallejo, Gustavo A. Madero, 07738 Ciudad de México, CDMX, México

CORREO ELECTRÓNICO: [miguel\\_sanchezbrito@hotmail.com](mailto:miguel_sanchezbrito@hotmail.com)

### Received:

11 September 2022

### Accepted:

3 December 2022

## INTRODUCTION

The vaccination strategy adopted by all countries has made it possible to reduce both the number of infected people and the mortality rate caused by the SARS-CoV-2 virus, however, the early detection of the coronavirus disease (COVID-19) caused by the virus is crucial to stop its spread <sup>[1]</sup>. Reverse transcriptase-polymerase chain reaction (RT-PCR) is the first-line test to diagnose this disease, which uses different specimens: blood, serum, plasma, urine, nasopharyngeal aspirate, oropharyngeal swab, sputum, and saliva principally <sup>[2]</sup> <sup>[3]</sup> <sup>[4]</sup> <sup>[5]</sup> <sup>[6]</sup> <sup>[7]</sup> <sup>[8]</sup>. Depending on the chosen specimen and the biomarkers that will be used, this technique could take up to 100 minutes approximately <sup>[5]</sup>, highlighting that the specimens that have reported the best sensitivity and specificity (more than 90 % in both parameters if the test is performed approximately five days after infection) are oropharyngeal and nasopharyngeal swab samples <sup>[5]</sup>. In addition to these types of samples, it has been reported that it is possible to obtain similar percentages by analyzing sputum <sup>[2]</sup> <sup>[3]</sup> <sup>[6]</sup> <sup>[8]</sup>.

Despite the promising results obtained by RT-PCR in the diagnosis of COVID-19, factors such as the incubation time of the virus, the processing time of the sample to obtain results, and price associated with the test have encouraged the search for different methodologies that could be used in great population as screening, avoiding the spread of the virus <sup>[7]</sup> <sup>[9]</sup> <sup>[10]</sup>.

Fourier transform infrared (FTIR) spectroscopy reveals the chemical bonds of the molecules that make up a sample thanks to the impact with an electromagnetic frequency (Hertz) belonging to the mid-infrared (IR) region. The vibrations produced and the frequency that caused them are recorded in a two-dimensional matrix known as an FTIR spectrum. Several regions have already been identified on the IR spectrum depending on the molecules that make up the sample (lipids, proteins, nucleic acids, among others) <sup>[11]</sup> <sup>[12]</sup> <sup>[13]</sup>.

Despite the above, the main drawback not only of FTIR spectroscopy, but of many others, is the signals overlapping. The more components that make up the sample that is analyzed, the greater the probability that these components present a chemical bond in common, which causes overlap between the populations that are studied, reason by which machine learning techniques are being used, making possible to solve this limitation thanks to the interpolation to a dimensional region different from the one posed by the original problem (in the support vector machine case). This approach has also been adopted by the authors of <sup>[14]</sup> <sup>[15]</sup> <sup>[16]</sup> <sup>[17]</sup> <sup>[18]</sup>.

In <sup>[14]</sup>, authors propose a strategy based on multivariate-partial least squares (PLS) associated with k-nearest neighbors (KNN) to characterize 243 samples of oropharyngeal swab suspension fluid. The strategy proposed by the authors allowed them to report 87 % sensitivity, 66 % specificity, and 78.4 % accuracy. Although their study focused only on the female population during pregnancy and analyzing blood samples, authors of <sup>[15]</sup>, report an accuracy greater than 90 % in the characterization of 37 samples of participating patients considering a model based on the C5.0 single decision tree algorithm and deep neural network approach. Similar to <sup>[15]</sup>, the authors of <sup>[16]</sup>, analyze serum samples of 249 patients through ATR-FTIR and multivariate linear regression model (MLRM), allowing to report sensitivity and specificity values of 94.55 % and 98.44 % respectively. Analyzing sera samples from 82 patients, the authors of <sup>[17]</sup>, propose a mathematical model based on Partial least squares and discriminant analysis (PLS-DA). With the PLS-DA model, the authors were able to report a sensitivity of 100 % and a specificity of 87.5 %. Finally, in <sup>[18]</sup>, the authors present a strategy that allows obtaining values of 97.8 % accuracy, 97 % sensitivity and 98.3 % specificity, analyzing FTIR spectra of ribonucleic acid (RNA) from 280 patients. The results reported in their work were obtained thanks to the application of different ML strategies, which were applied as follows: they use dimension reduction techniques, namely principal component anal-

ysis (PCA), partial least square (PLS) and Sparse Classification and then use logistic regression for PCA and PLS and support vector machine (SVM) and kernel SVM for classification.

In this sense, in the present work, we evaluate the performance of different Machine Learning (ML) techniques, in order to identify the one that would allow the best results to be obtained for the characterization of 1275 Attenuated Total Reflection (ATR)-FTIR saliva spectra, of which 66 were previously confirmed as carriers of the SARS-CoV-2 virus and the rest were reliably assigned to the control group since their samples were obtained and processed during the year 2019, a period in which no case of infection by this virus had been reported in Mexico. Our results suggest that the best strategy is multivariable linear regression (MLRM), since considering Leave-One-Out-Cross Validation (LOOCV) and Hold-Out cross validation segmentations, it is possible to correctly identify the spectra of each of the populations.

## MATERIALS AND METHODS

This section describes the strategies for taking samples, capturing the ATR-FTIR spectrum, its pre-processing and analysis.

### Samples acquisition

For the control group conformation, 1209 healthy volunteers were recruited in the “*Unidad de Especialidades Médicas (UEM)*” of the National Defense Ministry-Mexico from February 2019 to February 2020 (a period in which the COVID-19 has not reached Mexico borders), following what is stated in the protocol with internal folio: 001/2019 and presented to the clinical research committee of the UEM. For COVID-19 samples, in the period of May and June 2020, after the approval of the research project with official number: C.INV.-034, 66 persons positive to COVID-19 were recruited in the “*Hospital Central Militar*” of the National Defense Ministry-Mexico, who were diagnosed through RT-PCR technique; the days elapsed from COVID-19

diagnosis to saliva sampling range from 1 to 30 days with a mean of  $11 \pm 7$  days.

Volunteers donated approximately 1 ml of saliva, collected in sterile 1.5 ml microcentrifuge tubes. After being collected, the samples were refrigerated at a temperature between 0 and 4 °C until its spectrum was captured as suggested in [13] [19] [20]. In order to participate in this research project, the volunteers should have reached the age of majority (18 years in Mexico) and have a fasting period of at least 8 hours. In addition, in order not to add external components to the saliva sample, the participants did not have to previously wash the oral cavity, nor had any dental treatment. The healthy patients were informed that their samples would be used for different diagnostic assays as a reference control, and the COVID-19 patients were informed that their samples would be used to try other types of diagnosis. In order to reduce the effect of sample degradation caused by bacteria, between 10 and 15 patients were sampled each day. In this way, the period between the time the sample was obtained and its processing by FTIR spectroscopy did not exceed 1 hour, since, as [19] suggests, even when stored at -80 °C, the degradation process affects the nature of the biological specimens analyzed by FTIR spectroscopy.

The research protocols were evaluated and approved by the research committees of the UEM and the *Hospital Central Militar*. All the experiments carried out with the samples obtained with the informed consent of the volunteers were developed considering the provisions of the Helsinki Treaty.

### Spectra capture

To capture the spectrum, 3  $\mu$ l were collected by pipetting and subjected to a drying process. Subsequently and using the Jasco FTIR-6600, the absorbance spectrum was captured through the attenuated total reflectance (ATR) sampling mode, with a resolution of 4  $\text{cm}^{-1}$ , and 120 scans were performed as suggested for liquid samples [11] [12]. Once the sample was dry, it was possible

to appreciate the main biological macromolecules reported [13] [21] [22], such as lipids (L) in the region of 3000-2800  $\text{cm}^{-1}$ , amide I and II proteins (P) in the range of 1700-1600 and 1560-1500  $\text{cm}^{-1}$  respectively, and nucleic acids (NA) in the region at 1250-1000  $\text{cm}^{-1}$ .

The personnel in charge of collecting and processing the samples were equipped with the necessary protective equipment to guarantee their safety. Once the spectrum of the sample was captured, both the laboratory and the material where the processing was carried out were sanitized using type C ultraviolet light.

### Sample pre-processing

Before the analysis of the saliva spectra, these were normalized using the Standard Normal Variate (SNV) methodology as indicated Equation (1):

$$SNV = \frac{x - \mu}{\sigma} \quad (1)$$

x: spectrum absorbance

$\mu$ : mean

$\sigma$ : standard deviation

### Classification and validation models

In the search for alternative strategies to characterize FTIR spectra of patients with diabetes, dengue, different types of cancer and Parkinson's disease, different ML strategies have performed better than others [23] [24] [25] [26]. Analyzing this type of signals, according to the authors of [20] [27], the classification methods that allow the best results to be obtained are linear discriminant analysis (LDA), quadratic discriminant analysis (QDA), partial least squares regression discriminant analysis (PLS-DA), K-nearest neighbors (KNN), support vector machines (SVMs), and artificial neural networks (ANNs), so, in the present work, we evaluate the performance of ANNs (classification and regression), SVMs (classification and regression), KNN, and LDA, in addition to a multivariate linear regression model (MLRM). The initial conditions of the methodologies are presented below:

ANNs: A simple perceptron with hyperbolic tangent as

an activation function, Equation (2).

$$\tanh(x) = \frac{\sinh(x)}{\cosh(x)} \quad (2)$$

SVM: A support vector machine, Equation (3), using a 2 degree polynomial kernel ( $d=2$ ), Equation (4).

$$\begin{aligned} \min 0.5 \|\underline{w}\|^2 + C \sum_{i=0}^n \xi_i \\ \text{s.t. } y_i(\underline{w}^* \underline{x} - b) \geq 1 - \forall x_i \xi_i \geq 0 \\ \text{with } \xi = 0.1 \text{ and} \end{aligned} \quad (3)$$

a tolerance of termination criterion of 0.001

$$(ax + b + r)^d \quad (4)$$

KNN: considering  $K=10$ . In this strategy, the closest  $k$  samples (10) to the evaluated one are considered, and its membership will be the same as that of most of the  $K$  neighbors considered. The closeness between the samples was calculated by means of the Euclidean distance formula, exposed in Equation (5)

$$DE = \sqrt{(x_2 - x_1)^2 + (y_2 - y_1)^2} \quad (5)$$

LDA: with a tolerance= 1.0, based on Bayes probability theorem:  $p(x|Covid)$  and  $p(x|Control)$ , assigning a category to a new sample according to the one that allows obtaining the highest probability based on its attributes (absorbance values).

MLRM: A multivariate linear regression model of the form Equation (6), where  $b$ =interceptor,  $m_i$ =slope,  $X_i$ =independent variable  $i$  and  $\varepsilon$  is the error value.

$$Y_i = b + m_1 x_1 + \dots + m_n x_n + \varepsilon \quad (6)$$

The accuracy Equation (7), sensitivity Equation (8), and specificity Equation (9) of the ML models, was evaluated considering leave-one-out cross-validation (LOOCV) methodology [28], and due to the number of samples, the Kolmogorov-Smirnov technique was used to evaluate the normality of the spectra [29]. We, additionally, use LOOCV to choose the best ML methodology and the best spectra sub-region to characterize the



control group and the COVID-19 group. Once regions and the methodology were selected, the ML classifier's performance was evaluated through a Hold-Out methodology with 20 % of each population (control and COVID-19) considered in the evaluation process and the remaining 80 % of the spectra for the training task as [30][31][32] suggest. The samples were randomly selected.

$$Accuracy = \frac{TP+TN}{TP+FP+TN+FN} \quad (7)$$

$$Sensitivity = \frac{TP}{TP+FN} * 100 \quad (8)$$

$$Specificity = \frac{TN}{TN+FP} * 100 \quad (9)$$

In Equations (7), (8), (9), TP= true positives, TN= true negatives, FP=false positives, and FN=false negatives. We employ the determination coefficient  $r^2$ , Equation (10), to evaluate the performance of regression models against the dependent variable.

$$r^2 = 1 - \frac{\text{sum of squares regression}}{\text{sum of squares total}} \quad (10)$$

Both the ML models and the validation strategies presented in Equations 1-10 were developed in the c++ programming language via the Xcode integrated development environment for macOS. The equipment used was a MacBook Air with an Apple M1 chip and 8 GB RAM.

## RESULTS AND DISCUSSION

Through ANN (for classification and regression), SVM (for classification and regression), KNN, LDA, and MLRM, we evaluate the feasibility to identify positive COVID-19 patients from healthy persons. The database was constituted by  $n= 1275$ , obtained from 1209 healthy persons and 66 COVID-19 patients. The gender and age of the patients are presented in Table 1.

The evolution from the disease diagnosis to the taking of samples is shown in Figure 1; it is possible to appreciate that the days of the infection evolution of the majority of the population was between 5 and 10 days, the period in which the highest efficacy of PCR test is re-

ported [7][9]. Besides, it is possible to observe that a large part of our population was diagnosed between 1-4 days and 11-30 days after infection.

TABLE 1. Information of the patients analyzed.

Patients			
Population	Gender	Samples	Age $\pm$ SD
Healthy	Male	496	60.5 $\pm$ 8.6
	Females	713	
COVID-19	Male	54	51.3 $\pm$ 12.8
	Females	12	

\*SD: Standard deviation.

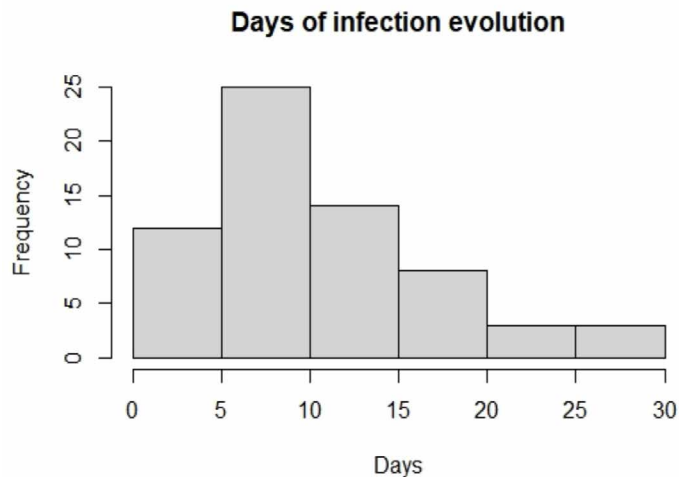
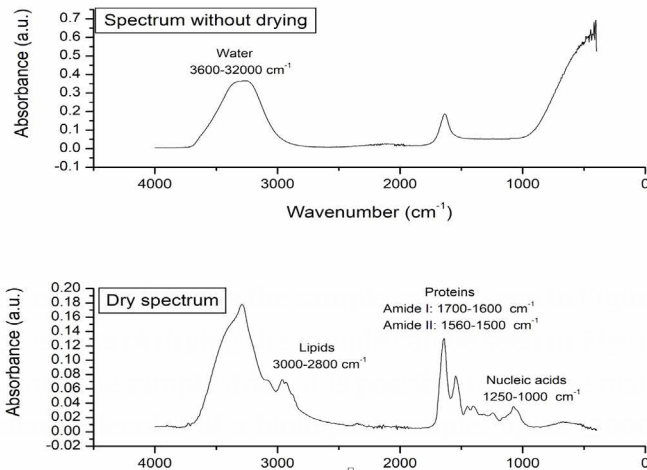


FIGURE 1. Evolution of infection from formal diagnosis to sample collection.

The effects of drying the sample can be seen in Figure 2, once the sample dries, it is possible to see the main macromolecules of a biological sample: lipids (3000-2800  $\text{cm}^{-1}$ ), proteins (1700-1600  $\text{cm}^{-1}$  and 1560-1500  $\text{cm}^{-1}$  where vibrations associated with amides I and II are reported), and nucleic acids (1250-1000  $\text{cm}^{-1}$ ) [13] [22].

To have a first indicator of the subregions that most contrast the populations, we average the spectra of each of the populations and compare them as shown in Figure 3, two types of differences between the populations were observed: in the amide protein regions (1700-1600  $\text{cm}^{-1}$  and 1560-1500  $\text{cm}^{-1}$ ), a consider-

able displacement in COVID-19 patients is observed, while in the nucleic acid, higher absorbance values in COVID-19 spectra are shown attributed to glycogen and other carbohydrates.



**FIGURE 2.** Morphological changes of the sample associated with the drying process. In the dry spectrum, the main macromolecules of a biological sample are indicated.

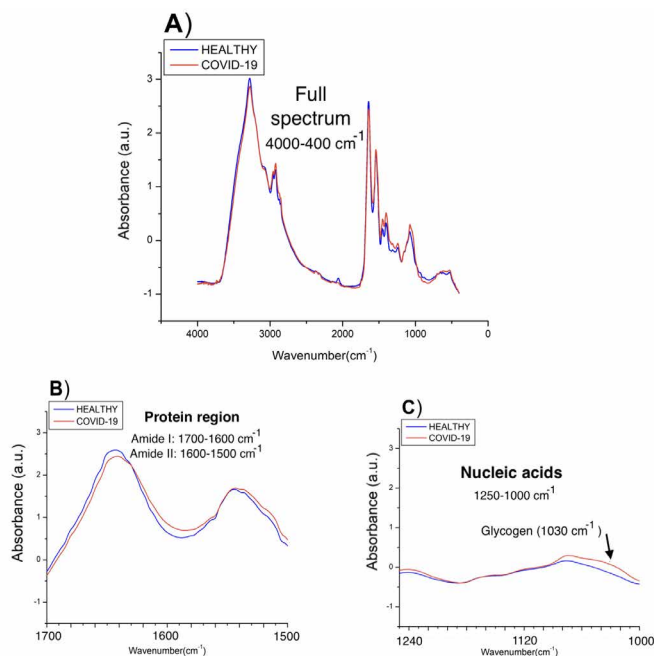


**FIGURE 3.** Spectra obtained from the medians of the absorbances of each population. A) Complete spectra in the mid-infrared region (4000-400  $\text{cm}^{-1}$ ), B) Proteins region (1700-1500  $\text{cm}^{-1}$ ), C) Nucleic acids region (1250-1000  $\text{cm}^{-1}$ ).

Using ANNs, SVMs, KNN, LDA, and MLRM we independently evaluate different regions of the FTIR spectrum, the full spectrum (4000-400  $\text{cm}^{-1}$ ), lipids (3000-2800  $\text{cm}^{-1}$ ), biological fingerprint (B.F., 1800-900  $\text{cm}^{-1}$ ) [20], amide I (1700-1600  $\text{cm}^{-1}$ ), amide II (1560-1500  $\text{cm}^{-1}$ ), and nucleic acids (1250-1000  $\text{cm}^{-1}$ ) to determine if it is possible to discriminate between both populations. Through LOOCV, we first determined the region that could be associated with the viral infection. Once the region and the machine learning technique allowed us to obtain the best results were identified, we used the Hold-Out methodology to evaluate the performance of the proposed methodology according to the size of samples that make up our database [30][31][32]. The results obtained are presented in the following subsections.

### ANNs performance

ANNs can be used to model regression (ANNr) and classification (ANNc) problems [30]. The main difference between both methodologies is the type of variable to be predicted, while in classification problems, the variable is categorical; in regression, it is numerical. After evaluating the different spectral regions by ANNr, we obtained the results presented in Figure 4, where it can be observed that using the entire spectrum, it is possible to build a regression model to characterize both populations.

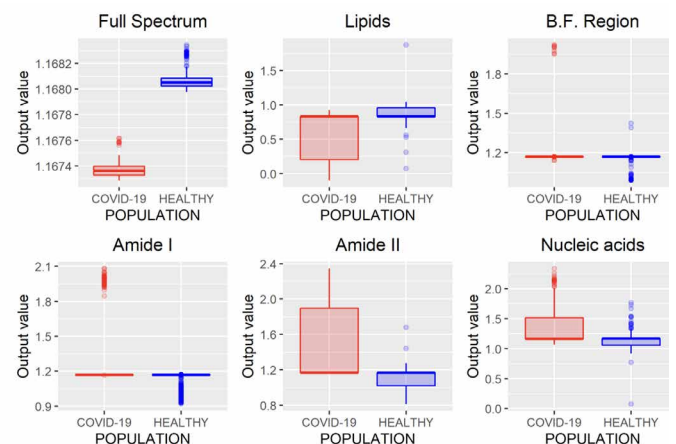


**FIGURE 4.** ANNr performance analyzing different regions of the FTIR spectrum (B.F., biological fingerprint region).

In Figure 5, the results using ANNc are observed, where it can be noticed that it is impossible to distinguish each population, unlike ANNr that allows characterizing both populations when the entire FTIR spectrum is analyzed (Figure 4).

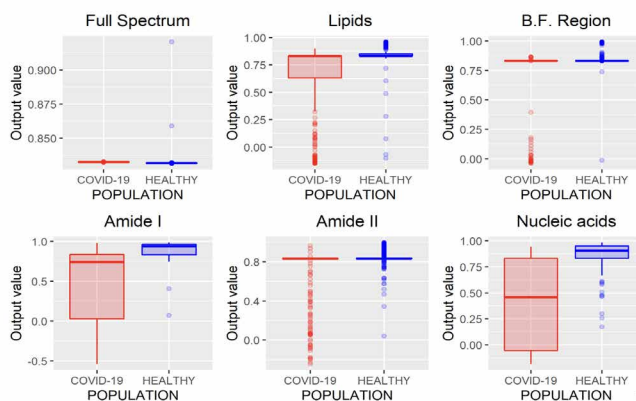


**FIGURE 5. ANNc performance analyzing different regions of the FTIR spectrum (B.F., biological fingerprint region).**

### SVMs performance

Similar to ANNs, SVMs allow developing regression (SVMr) and classification (SVMc) models. The results obtained through regression models are presented in Figure 6, where it is possible to note that analyzing the entire spectrum, the B.F. region, and amide I, both populations can be discriminated, highlighting that only one spectrum is misclassified in these three regions. Nevertheless, considering that amide I region employees have fewer variables (wavenumbers) than the full spectrum and nucleic acid region, it is of greater interest to use this region to contemplate the processing time.

Similarly, to SVMr, SVMc allows to obtain considerable results from the study of the complete spectrum, the B.F. and the region associated with amide I, Figure 7.

### KNN performance

KNN is a classification algorithm used to categorize objects based on their proximity to K nearest objects

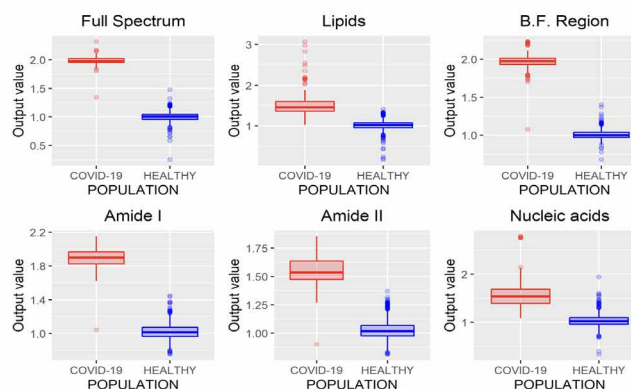


**FIGURE 6. SVMr performance analyzing different regions of the FTIR spectrum (B.F., biological fingerprint region).**

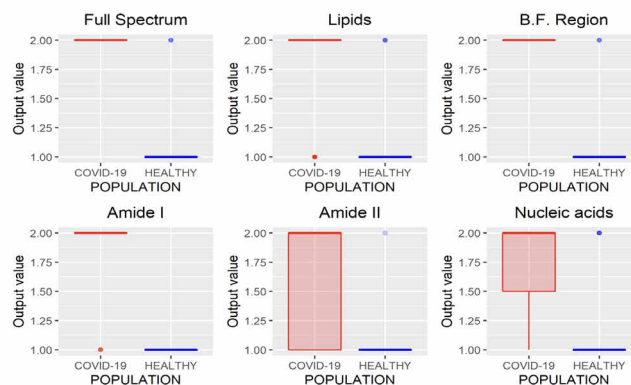


**FIGURE 7. SVMc performance analyzing different regions of the FTIR spectrum (B.F., biological fingerprint region)**

grouped in the training set [20]. The results obtained using this methodology are presented in Figure 8, where we can infer that the variations in the absorbances of the spectra of the same class make it difficult to use this technique in the task of characterizing populations from FTIR spectra of saliva samples since in all cases false positives were identified.

### LDA performance

LDA is a classification methodology also known as Fisher's linear discriminant (FLD). In this method, training and test sets are projected into the same subspace, and the similarities between these data sets are identified.

The results obtained by this technique are presented in Figure 9, where it is observed that using the B.F., it is possible to characterize the spectra correctly. Besides analyzing the amide I and II regions, good results were obtained since only eight and five infected patients were incorrectly identified as healthy patients.

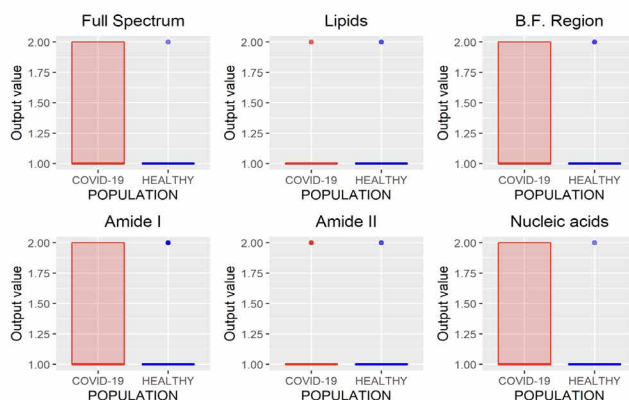


**FIGURE 8.** KNN performance analyzing different regions of the FTIR spectrum (B.F., biological fingerprint region).

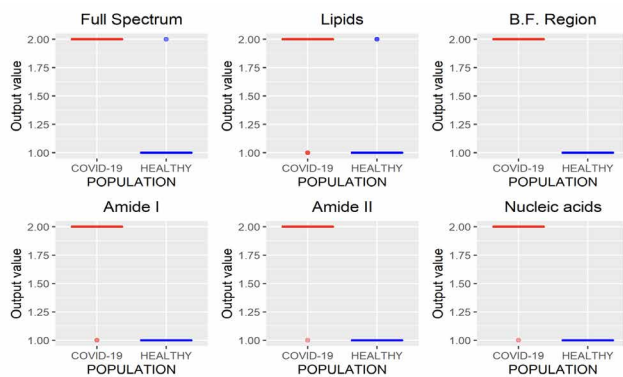


**FIGURE 9.** LDA performance analyzing different regions of the FTIR spectrum.

### MLRM performance

MLRM is a regression model based on a simple linear regression analysis with a difference that considers more than one independent variable to estimate the independent variable's value. In Figure 10, the results of MLRM are depicted; we can observe that it is possible to perform the characterization of the spectra reliably by analyzing the B.F., amide I, and amide II regions, allow-

ing one error. However, the results obtained using the amide I region showed a minor variance than those obtained by analyzing amide II; moreover, this region requires fewer variables concerning the B.F. region (1700 wavenumbers less), allowing the study less time.

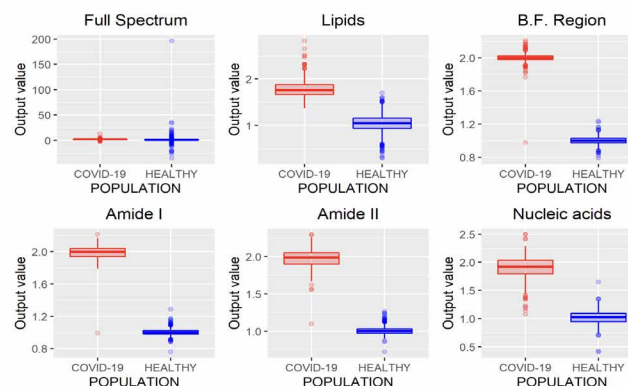


**FIGURE 10.** MLRM performance analyzing different regions of the FTIR spectrum.

Unlike regression models (ANNr, SVMr, MLRM), where the variables to be predicted are data with continuous values, classification models (ANNc, SVMc, KNN, LDA) restrict the use of the variable to be predicted, since being categorical, it is not possible to use them to solve a system of equations as in regression models. Although in Figures 5, 7, 8, 9, where the results of the evaluation of classification models are presented, it is possible to see numerical data on the abscissa axis when COVID-19 or HEALTHY should only appear, it was defined that, for its graphing, the value of 1 was adopted for a prediction associated with the HEALTHY group by the classification model and 2 for a COVID-19 prediction, the above due to the fact that the function used for plotting implemented through the `#include <QBoxPlotSeries>` library in the `c++` language requires a numerical value on this axis. Figures 4-10 present the results obtained by the different classification/regression methods previously mentioned using the LOOCV methodology employing box plots. The purpose of the exercise is to select the technique that allows the best possible distance between both populations (COVID-19 and healthy) on the

vertical axis, analyzing either the entire spectrum or a subregion of the spectrum. Considering the above, we can observe that the best options obtained to identify the populations using the least possible information are SVMr and MLRM since only one error was obtained by analyzing only the region associated with amide I ( $1700\text{-}1600\text{ cm}^{-1}$ ).

Table 2 summarizes the behavior of both methodologies (SVMr and MLRM), analyzing the amide I ( $1700\text{-}1600\text{ cm}^{-1}$ ) region. It is possible to observe that there is a COVID-19 spectrum wrongly categorized by both methodologies. Although it is possible to obtain similar accuracy, sensitivity, and specificity metrics for the analyzed database, both methodologies' performance is not the same. In Figure 11, we present the SVM and MLRM methodologies' output values' distribution, appreciating that both techniques erroneously classify a single spectrum of 1275 that make up the database. However, the MLRM output values' dispersion suggests that it is the most reliable method to correctly identify a COVID-19 positive patient.

**TABLE 2. Outputs ranges of the SVMr and MLRM methodologies for the 1275 spectra in the database using LOOCV.**

Algorithm behavior						
Method	Population	Output		A	Se	Sp
		Min	Max			
SVMr	COVID-19	1.04	2.14	99	98.5	100
	Healthy	0.75	1.44			
MLRM	COVID-19	0.99	2.21	99	98.5	100
	Healthy	0.75	1.28			

\*A: Accuracy, Se: Sensibility, Sp: Specificity.

Moreover, in Figure 11, we can see that the MLRM outputs presented are more compact for both populations concerning SVMr. In the same way, in Table 3, some statistical parameters obtained from the analysis of the output values of the methodologies, including determination coefficient ( $r^2$ ), are presented; highlighting that it is possible to obtain a regression model that

presents accuracy employing MLRM due to the  $r^2$  obtained. The outputs present a lower standard deviation that suggests that this technique will perform better with a more extensive database.

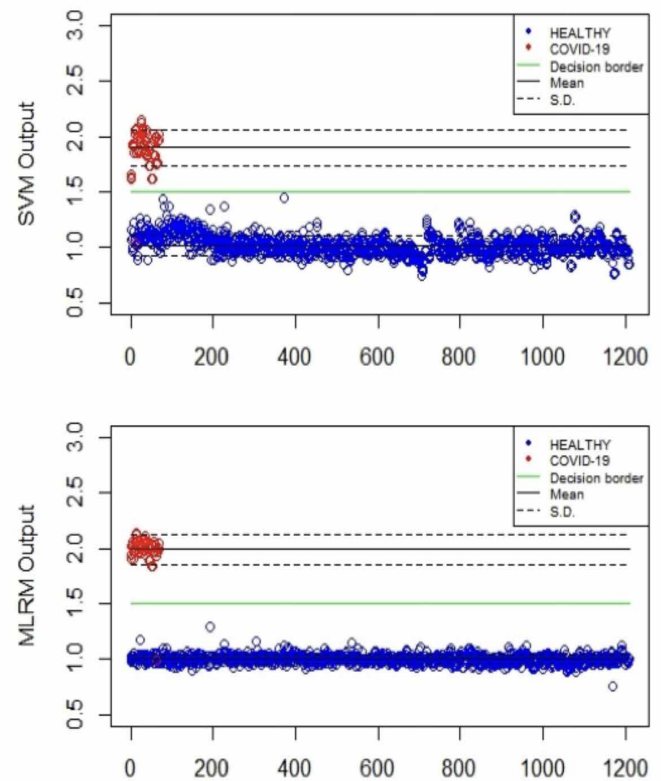


**FIGURE 11. Distribution of the SVM and MLRM techniques' output values analyzing the amide I region using LOOCV.**

**TABLE 3. Statistical analyses of SVMr and MLRM outputs obtained with a LOOCV methodology.**

Algorithm behavior					
Method	Population	Output		S.D.	$r^2$
		Min	Max		
SVMr	COVID-19	1.04	2.14	0.16	0.91
	Healthy	0.75	1.44	0.08	
MLRM	COVID-19	0.99	2.21	0.13	0.97
	Healthy	0.75	1.28	0.03	

\*S.D. : Standard deviation,  $r^2$ : determination coefficient.

Some authors have declared that employing a database with considerable numbers of samples, it is desirable to evaluate the model using random subset selection techniques in addition to LOOCV [20] [28] [30]. So, we also evaluate the performance of the MLRM considering only the amide I region through the Hold-Out methodology with a partition of 80 % of the spectra used in training (1020 spectrum), and 20 % (255, 242 belong to the control group and 13 to the COVID-19 group) in the evaluation process [28] [33]. To better understand the model's performance using this methodology, we repeat the exercise 6 times. The results are presented in Figure 12.

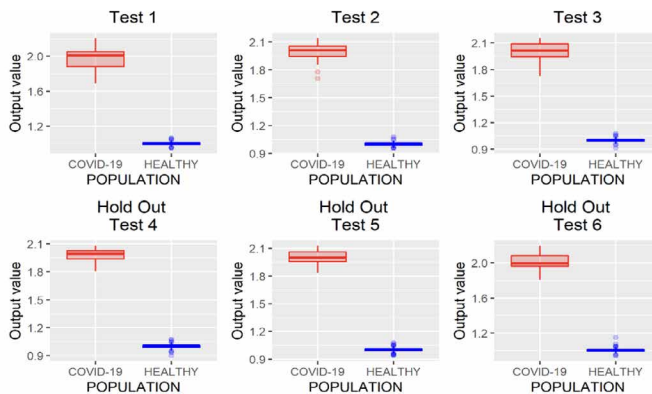


**FIGURE 12. MLRM performance analyzing different regions of the FTIR spectrum.**

From Figure 12, it is possible to infer that the use of MLRM will hold better results increasing the database spectra once the outputs of this regression method presented a considerable distance between them. According to [33] [34], the performance of machine learning techniques could be related to the number of samples that we provide them in the training process, so, to prove the performance of the MLRM model with a similar sample quantity than COVID-19 population, we randomly select 66 samples of the control group and evaluate its accuracy through hold out, we repeated this exercise 6 times and the results are presented in Figure 13, the outputs of the MLRM model when a virus carrier spectra is evaluated are presented in red points, while the non-infected samples are shown in

blue points; it is possible to appreciate that the accuracy, similar to the result presented in Figure 12 with all the samples in control group (1207) still is 100 %.

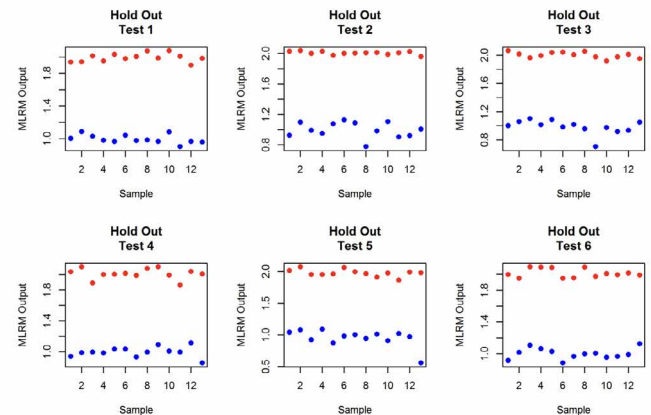


**FIGURE 13. MLRM hold out performance for a similar sample quantity.**

**TABLE 4. Statistical analyses of MLRM outputs obtained with a Hold Out methodology.**

Algorithm behavior				
Iteration	Population	Output		S.D.
		Min	Max	
1	COVID-19	1.90	2.07	0.0517
	CONTROL	0.90	1.087	0.0525
2	COVID-19	1.96	2.03	0.0215
	CONTROL	0.77	1.12	0.101
3	COVID-19	1.92	2.06	0.0427
	CONTROL	0.71	1.09	0.101
4	COVID-19	1.86	2.0	0.0700
	CONTROL	0.85	1.11	0.067
5	COVID-19	1.86	2.07	0.055
	CONTROL	0.55	1.08	0.135
6	COVID-19	1.95	2.09	0.0558
	CONTROL	0.88	1.12	0.0690

\*S.D.: Standard deviation.

The statistical analysis of the 6 exercises presented in Figure 13 are reported in Table 4; this table shown that

despite the variance observed in the standard deviation (S.D.) of the control group, the distance between means and outputs values of both population turn-on the characterization of possible virus carriers reliable. Regarding the performance of the MLRM model for the training subset, we present Figure 14, it is possible to observe that as for the evaluation subset, the performance of the model is optimal. It is noted that not only the samples were correctly identified, but also that the separability between the populations is similar to that achieved in the evaluation process.

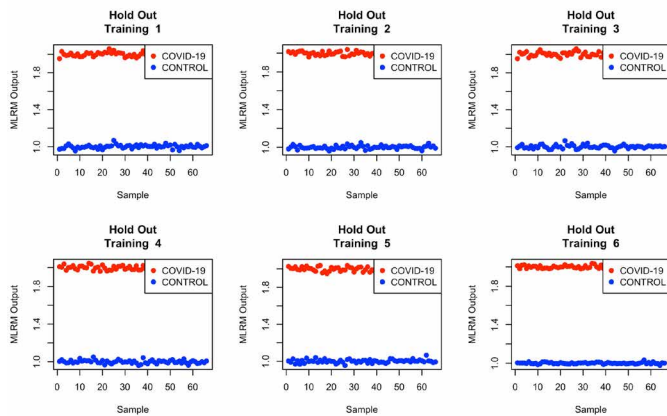


**FIGURE 14. MLRM hold out performance for a similar sample quantity in the training process.**

Table 5 shows the output values for each iteration evaluating the training subset.

Considering the ranges of output values for the MLRM model shown in Table 5, it is possible to conclude that, evaluating the training subset, there is no overlap between the results.

The easy spread of SARS-CoV-2 and the lack of effective treatment and diagnosis methodology have contributed to seeking diagnostic methods to avoid the virus's spread. Despite the PCR technique has been adopted as the most reliable diagnosis methodology [2] [3] [4] [5] [8] [9], as previously mentioned, its most significant challenge is the detection of people infected at early stages. Moreover, it cannot be used as a screening diagnosis technique in great populations due to its high cost and

specialized personal needs. Herein, we present a novel methodology to detect people positive to COVID-19. Our methodology is based on the analysis of the FTIR spectra of saliva samples using machine learning techniques.

In contrast to PCR that punctually detects the gene associated with a particular viral infection, the FTIR technique allows detecting the bonds of a sample's molecular components through its interaction with different electromagnetic frequencies [11] [12]. The intersection of the same bonds of all sample components has made it difficult to use this clinical diagnosis technique because of the need for complex mathematical models to find a specific spectral behavior attributable to pathology. To deal with this problem, some researchers have already coupled FTIR with machine learning in order to characterize populations with SARS-CoV-2 [14] [15] [16] [17] [18].

In the same way as [16] [18], the results obtained in this research work suggest that MLRM and SVMr turn out to be the best options to characterize FTIR spectra of patients with and without COVID-19 although the analyzed samples differ. Despite the fact that the good results presented by the authors of the aforementioned works would allow the development of a robust strategy for a preliminary analysis of possible carriers of the virus, the nature of the samples analyzed, serum and RNA respectively, involve specialized personnel and reagents to process the samples are necessary in contrast to the method described here. It is also necessary to consider the hypothesis that the difference in the percentages of accuracy, sensitivity, and specificity, despite using similar strategies between [16] [18] and the present one, could be attributed to storage time, since the authors of, report having stored the specimens for a period longer than that considered in this work.

The results achieved in this work, could open a window for the development of an electronic device that allows identifying patients infected by the virus in a

non-invasive way. Such a device could have a good performance considering only the frequencies associated with the wavenumbers ( $1700\text{-}1600\text{ cm}^{-1}$ ) attributed to amide I, since as Figures 10-13 indicate, it is where the MLRM model has better performance.

**TABLE 5. Statistical analyses of MLRM outputs obtained with a Hold Out methodology in the training process.**

Algorithm behavior				
Iteration	Population	Output		S.D.
		Min	Max	
1	COVID-19	1.953	2.059	0.02210
	CONTROL	0.9534	1.068	0.01948
2	COVID-19	1.9574	2.0447	0.0202
	CONTROL	0.9612	1.050	0.01757
3	COVID-19	1.949	2.0607	0.0243
	CONTROL	0.9545	1.0655	0.0186
4	COVID-19	1.957	2.044	0.02021
	CONTROL	0.9612	1.0508	0.0175
5	COVID-19	1.9494	2.0607	0.0243
	CONTROL	0.9545	1.065	0.0186
6	COVID-19	1.959	2.0372	0.0151
	CONTROL	0.9761	1.033	0.00839

\*S.D.: Standard deviation.

## CONCLUSIONS

In this work, we evaluate the performance of different classification techniques to propose an agile, reliable, non-invasive, and cheap methodology. For this purpose, we analyze the FTIR spectra of saliva samples. After analyzing six different regions of each one of the 1275 spectra that make up our database with four different classification techniques commonly used in the machine learning area, we conclude that it is possible to characterize both populations by analyzing the amide I region ( $1700\text{-}1600\text{ cm}^{-1}$ ) through MLRM, showing percentages of accuracy, sensitivity, and specificity of 99%, 98.5 %, and 100 %, respectively.

Considering that the disparity in terms of samples could be a factor that masked the effectiveness of the proposed method, 6 sub-databases of the control group were created with the same number of samples as the covid group (66). The results presented in Figure 13 and Table 4 and 5 confirm the effectiveness of the proposed method. Additionally, the distance between the populations as well as the proximity between the results obtained when evaluating samples from the same population by means of MLRM suggest that the proposed method has great possibilities of being applied in a real environment.

However, it is essential to mention that more research needs to be done focusing on each band or region's description to determine if the observed changes are associated with the virus itself or immune response. Also, it is essential to train and evaluate the performance of the model with spectra captured through other spectrometers, this would allow making models that circumvent the noise that the materials could cause. Moreover, it is necessary to increase the positive COVID-19 population to strengthen the results shown in this research.

## AUTHOR CONTRIBUTIONS

G.J.V.Z. conceptualized the project, participated in all the writing stages of the manuscript (preparation of the original draft, review and edition of the different versions and the final document), contributed to the sample collection and processing. M.M.M.M. conceptualized the project, participated in all the writing stages of the manuscript (preparation of the original draft, review and edition of the different versions and the final document), contributed to the sample collection and processing. A.M.C. wrote, reviewed and edited the different versions of the manuscript, and contributed to the sample collection and processing. F.G.G. wrote, reviewed and edited the different versions of the manuscript, contributed to the sample collection and processing. M.G.R. contributed to the sample collection and processing. M.S.B. conceptualized the project,



designed the experiments, wrote, reviewed and edited the different versions of the manuscript, contributed to the sample collection and processing. All authors reviewed and approved the final version of the manuscript.

### **Acknowledgment**

We appreciate the support of the participating patients, who despite the illnesses caused by the virus decided to support the research project by donating a saliva sample. Equally important for the realization of the project is the A022-2021 (SEDENA) budgetary program.

## REFERENCES

- [1] World Health Organization. Coronavirus disease (COVID-19) [Internet]. 2021. Available from: <https://www.who.int/health-topics/coronavirus>
- [2] To KKW, Tsang OTY, Leung WS, Tam AR, et al. Temporal profiles of viral load in posterior oropharyngeal saliva samples and serum antibody responses during infection by SARS-CoV-2: an observational cohort study. *Lancet Infect Dis* [Internet]. 2020;20(5):565-574. Available from: [https://doi.org/10.1016/S1473-3099\(20\)30196-1](https://doi.org/10.1016/S1473-3099(20)30196-1)
- [3] To KKW, Tsang OTY, Yip CCY, Chan KH, et al. Consistent Detection of 2019 Novel Coronavirus in Saliva. *Clin Infect Dis* [Internet]. 2020;71(15):841-843. Available from: <https://doi.org/10.1093/cid/ciaa149>
- [4] Long C, Xu H, Shen Q, Zhang X, et al. Diagnosis of the Coronavirus disease (COVID-19): rRT-PCR or CT? *Eur J Radiol* [Internet]. 2020;126(1):108961. Available: <https://doi.org/10.1016/j.ejrad.2020.108961>
- [5] Ravi N, Cortade DL, Ng E, Wang SX. Diagnostics for SARS-CoV-2 detection: A comprehensive review of the FDA-EUA COVID-19 testing landscape. *Biosens Bioelectron* [Internet]. 2020;165:112454. Available from: <https://doi.org/10.1016/j.bios.2020.112454>
- [6] Zhang W, Du RH, Li B, Zheng XS, et al. Molecular and serological investigation of 2019-nCoV infected patients: implication of multiple shedding routes. *Emerg Microbes Infect* [Internet]. 2020;9(1):386-389. Available from: <https://doi.org/10.1080/22221751.2020.1729071>
- [7] Böger B, Fachi MM, Vilhena RO, Cobre AF, et al. Systematic review with meta-analysis of the accuracy of diagnostic tests for COVID-19. *Am J Infect Control* [Internet]. 2021;49(1):21-29. Available from: <https://doi.org/10.1016/j.ajic.2020.07.011>
- [8] Farshidfar N, Hamedani S. The Potential Role of Smart phone-Based Microfluidic Systems for Rapid Detection of COVID-19 Using Saliva Specimen. *Mol Diagn Ther* [Internet]. 2020;24:371-373. Available from: <https://doi.org/10.1007/s40291-020-00477-4>
- [9] Kucirka LM, Lauer SA, Laeyendecker O, Boon D, et al. Variation in False-Negative Rate of Reverse Transcriptase Polymerase Chain Reaction-Based SARS-CoV-2 Tests by Time Since Exposure. *Ann Intern Med* [Internet]. 2020;173(4):262-267. Available from: <https://doi.org/10.7326/M20-1495>
- [10] Luhby T. A coronavirus test could cost as little as \$20 or as much as \$850. *CNN* [Internet]. 2020. Available from: <https://edition.cnn.com/2020/07/15/health/coronavirus-test-cost/index.html>
- [11] Smith B. *Fundamentals of Fourier Transform Infrared Spectroscopy*. 2nd ed. Florida: Taylor and Francis Group; 2011. 1-17 p.
- [12] Smith BC. *Infrared Spectral Interpretation: A Systematic Approach*. United States of America: CRC Press; 1998. 304 p.
- [13] Bel'skaya LV, Sarf EA, Kosenok VK. Age and gender characteristics of the biochemical composition of saliva: Correlations with the composition of blood plasma. *J Oral Biol Craniofacial Res* [Internet]. 2020;10(2):59-65. Available from: <https://doi.org/10.1016/j.jobcr.2020.02.004>
- [14] Nogueira MS, Leal LB, Marcarini WD, Pimentel RL, et al. Rapid diagnosis of COVID-19 using FT-IR ATR spectroscopy and machine learning. *Sci Rep* [Internet]. 2021;11:15409. Available from: <https://doi.org/10.1038/s41598-021-93511-2>
- [15] Guleken Z, Jakubczyk P, Wiesław P, Krzysztof P, et al. Characterization of Covid-19 infected pregnant women sera using laboratory indexes, vibrational spectroscopy, and machine learning classifications. *Talanta* [Internet]. 2022;237:122916. Available from: <https://doi.org/10.1016/j.talanta.2021.122916>
- [16] Calvo-Gomez O, Calvo H, Cedillo-Barrón L, Vivanco-Cid H, et al. Potential of ATR-FTIR-Chemometrics in Covid-19: Disease Recognition. *ACS Omega* [Internet]. 2022;7(35):30756-30767. Available from: <https://doi.org/10.1021/acsomega.2c01374>
- [17] Bandeira CCS, Madureira KCM, Rossi MB, Gallo JF, et al. Micro-Fourier-transform infrared reflectance spectroscopy as tool for probing IgG glycosylation in COVID-19 patients. *Sci Rep* [Internet]. 2022;12:4269. Available from: <https://doi.org/10.1038/s41598-022-08156-6>
- [18] Kitane DL, Loukman S, Marchoudi N, Fernandez-Galiana A, et al. A simple and fast spectroscopy-based technique for Covid-19 diagnosis. *Sci Rep* [Internet]. 2021;11:16740. Available from: <https://doi.org/10.1038/s41598-021-95568-5>
- [19] Baker MJ, Trevisan J, Bassan P, Bhargava R, et al. Using Fourier transform IR spectroscopy to analyze biological materials. *Nat Protoc* [Internet]. 2014;9(8): 1771-1791. Available from: <https://doi.org/10.1038/nprot.2014.110>
- [20] Morais CLM, Lima KMG, Singh M, Martin FL. Tutorial: multivariate classification for vibrational spectroscopy in biological samples. *Nat Protoc* [Internet]. 2020;15:2143-2162. Available from: <https://doi.org/10.1038/s41596-020-0322-8>
- [21] Callery EL, Morais CLM, Paraskevaidi M, Brusci V, et al. New approach to investigate Common Variable Immunodeficiency patients using spectrochemical analysis of blood. *Sci Rep* [Internet]. 2019;9:7239. Available from: <https://doi.org/10.1038/s41598-019-43196-5>
- [22] Shi L, Liu X, Shi L, Stinson HT, et al. Mid-infrared metabolic imaging with vibrational probes. *Nat Methods* [Internet]. 2020;17:844-851. Available from: <https://doi.org/10.1038/s41592-020-0883-z>
- [23] Yang X, Fang T, Li Y, Guo L, et al. Pre-diabetes diagnosis based on ATR-FTIR spectroscopy combined with CART and XGBoots. *Optik* [Internet]. 2019;180:189-198. Available from: <https://doi.org/10.1016/j.ijleo.2018.11.059>
- [24] Lu Y, Zhao Y, Zhu Y, Xu X, et al. In situ research and diagnosis of breast cancer by using HOF-ATR-FTIR spectroscopy. *Spectrochim Acta A Mol Biomol Spectrosc* [Internet]. 2020;235:118178. Available from: <https://doi.org/10.1016/j.saa.2020.118178>
- [25] Naseer K, Ali S, Mubarak S, Hussain I, et al. FTIR spectroscopy of freeze-dried human sera as a novel approach for dengue diagnosis. *Infrared Phys Technol* [Internet]. 2019;102:102998. Available from: <https://doi.org/10.1016/j.infrared.2019.102998>
- [26] Wang X, Wu Q, Li C, Zhou Y, et al. A study of Parkinson's disease

- patients' serum using FTIR spectroscopy. *Infrared Phys Technol* [Internet]. 2020;106:103279. Available from: <https://doi.org/10.1016/j.infrared.2020.103279>
- [27] Sala A, Anderson DJ, Brennan PM, Butler HJ, et al. Biofluid diagnostics by FTIR spectroscopy: A platform technology for cancer detection *Cancer Lett* [Internet]. 2020;477:122-130. Available from: <https://doi.org/10.1016/j.canlet.2020.02.020>
- [28] Jarvis S, Crossley SA. Approaching Language Transfer Through Text Classification: Explorations in the Detection-based Approach [Internet]. *Blue Ridge Summit: Multilingual Matters*; 2012. 208p. Available from: <https://doi.org/10.21832/9781847696991>
- [29] Stewart WJ. *Probability, Markov Chains, Queues, and Simulation: The Mathematical Basis of Performance Modeling* [Internet]. New Jersey, United States: Princeton University Press; 2009. 776p. Available from: <https://doi.org/10.2307/j.ctvcn4gtc>
- [30] Paliouras G, Karkaletsis V, Spyropoulos CD (eds.). *Machine Learning and Its Applications: Advanced Lectures* [Internet]. Germany: Springer; 2001. 324p. Available from: <https://doi.org/10.1007/3-540-44673-7>
- [31] Hodeghatta UR, Nayak U. *Business Analytics Using R - A Practical Approach*. United States: Apress; 2016. 297p.
- [32] Vidgen R, Kirshner S, Tan F. *Business Analytics: A Management Approach*. United Kingdom: Bloomsbury Academic; 2019. 430p.
- [33] Géron A. *Hands-On Machine Learning with Scikit-Learn, Keras, and TensorFlow: Concepts, Tools, and Techniques to Build Intelligent Systems*. Canada: O'Reilly Media, Inc.; 2019. 851p.
- [34] Rajaguru H, Prabhakar SK. *KNN Classifier and K-Means Clustering for Robust Classification of Epilepsy from EEG Signals. A Detailed Analysis*. Germany: Anchor Academic Publishing; 2017. 54p.